Nucl. Fusion **53** (2013) 093024 (19pp) doi:10.1088/0029-5515/53/9/093024

Improved understanding of physics processes in pedestal structure, leading to improved predictive capability for ITER

R.J. Groebner[1], C.S. Chang[2], J.W. Hughes[3], R. Maingi[2], P.B. Snyder[1], X.Q. Xu[4], J.A. Boedo[5], D.P. Boyle[2], J.D. Callen[6], J.M. Canik[7], I. Cziegler[5], E.M. Davis[3], A. Diallo[2], P.H. Diamond[5], J.D. Elder[8], D.P. Eldon[5], D.R. Ernst[3], D.P. Fulton[9], M. Landreman[3], A.W. Leonard[1], J.D. Lore[7], T.H. Osborne[1], A.Y. Pankin[10], S.E. Parker[11], T.L. Rhodes[12], S.P. Smith[1], A.C. Sontag[7], W.M. Stacey[13], J. Walk[3], W. Wan[11], E.H.-J. Wang[4], J.G. Watkins[14], A.E. White[3], D.G. Whyte[3], Z. Yan[6], E.A. Belli[1], B.D. Bray[1], J. Candy[1], R.M. Churchill[3], T.M. Deterly[1], E.J. Doyle[12], M.E. Fenstermacher[4], N.M. Ferraro[1], A.E. Hubbard[3], I. Joseph[4], J.E. Kinsey[1], B. LaBombard[3], C.J. Lasnier[4], Z. Lin[9], B.L. Lipschultz[3], C. Liu[1], Y. Ma[3], G.R. McKee[6], D.M. Ponce[1], J.C. Rost[3], L. Schmitz[12], G.M. Staebler[1], L.E. Sugiyama[3], J.L. Terry[3], M.V. Umansky[4], R.E. Waltz[1], S.M. Wolfe[3], L. Zeng[12] and S.J. Zweben[2]

[1] General Atomics, PO Box 85608, San Diego, CA 92186–5608, USA
[2] Princeton Plasma Physics Laboratory, PO Box 451, Princeton, NJ 08543-0451, USA
[3] Massachusetts Institute of Technology, 77 Massachusetts Avenue, Cambridge, MA 02139-4307 USA
[4] Lawrence Livermore National Laboratory, PO Box 808, Livermore, CA 94551, USA
[5] University of California San Diego, 9500 Gilman Dr., La Jolla, CA 92093, USA
[6] College of Engineering, University of Wisconsin, Madison, WI 53706-1390, USA
[7] Oak Ridge National Laboratory, PO Box 2008, Oak Ridge, TN 37831, USA
[8] Institute for Aerospace Studies, University of Toronto, Toronto, Ontario, M3H 576, Canada
[9] Department of Physics and Astronomy, University of California, Irvine, CA 92616–6050, USA
[10] Tech-X, Boulder, CO 80303, USA
[11] Department of Physics, University of Colorado Boulder, Boulder, CO 80309, USA
[12] Department of Physics and Astronomy, and PSTI, University of California, Los Angeles, CA 90095, USA
[13] Georgia Institute of Technology, Atlanta, GA 30332, USA
[14] Sandia National Laboratory, PO Box 5800, Albuquerque, NM 87185, USA

E-mail: groebner@fusion.gat.com

Received 28 February 2013, accepted for publication 26 July 2013
Published 21 August 2013
Online at stacks.iop.org/NF/53/093024

Abstract
Joint experiment/theory/modelling research has led to increased confidence in predictions of the pedestal height in ITER. This work was performed as part of a US Department of Energy Joint Research Target in FY11 to identify physics processes that control the H-mode pedestal structure. The study included experiments on C-Mod, DIII-D and NSTX as well as interpretation of experimental data with theory-based modelling codes. This work provides increased confidence in the ability of models for peeling–ballooning stability, bootstrap current, pedestal width and pedestal height scaling to make correct predictions, with some areas needing further work also being identified. A model for pedestal pressure height has made good predictions in existing machines for a range in pressure of a factor of 20. This provides a solid basis for predicting the maximum pedestal pressure height in ITER, which is found to be an extrapolation of a factor of 3 beyond the existing data set. Models were studied for a number of processes that are proposed to play a role in the pedestal n_e and T_e profiles. These processes include neoclassical transport, paleoclassical transport, electron temperature gradient turbulence and neutral fuelling. All of these processes may be important, with the importance being dependent on the plasma regime. Studies with several electromagnetic gyrokinetic codes show that the gradients in and on top of the pedestal can drive a number of instabilities.

(Some figures may appear in colour only in the online journal)

1. Introduction

The H-mode pedestal will have a profound effect on plasma performance in ITER [1], the Fusion National Science Facility (FNSF) [2] and other fusion machines. The pedestal will govern the performance both through the confinement of the pedestal itself and by providing an important boundary condition for core confinement; higher values of pedestal pressure provide higher values of core pressure. For successful operation of fusion machines, the characteristics of the pedestal must be optimized to simultaneously meet several criteria. These criteria include sufficient pedestal pressure, small or no edge localized modes (ELMs), shielding of impurities and the ability to be fuelled by gas puffing or pellet injection. A predictive pedestal capability is required to optimize and design operating scenarios in ITER and to assist in the design of future fusion machines so that the pedestal properties can be modelled realistically.

To assist with the development of predictive capability, the US Department of Energy established an activity in fiscal year 2011, called the FY11 Joint Research Target for Pedestal Physics (JRT), to foster an increased effort to study pedestal physics. This activity resulted in a coordinated effort between experiment, theory and modelling communities to identify and improve predictive capability for important physics processes controlling pedestal structure. A major goal of this work was to compare pedestal physics results on C-Mod, DIII-D and NSTX in order to discern physics common to all three devices. This was accomplished partly by performing coordinated experiments to study the pedestal on all three devices and by using the same set of software tools to analyze the pedestal data from the three devices. Another means to meet this goal was to use several simulation codes to model pedestal physics in two or all three of these devices.

This work has led to increased confidence that a paradigm for understanding the ultimate limits to the pedestal pressure profile, based on two different physics criteria, is correct. One criterion is that finite-n, ideal peeling–ballooning modes provide a global limit to pedestal pressure; the second is that smaller scale and more localized kinetic ballooning modes (KBMs) provide a limit to the pedestal pressure gradient. Both of these physics processes are controlled by the interplay between the pressure profile and the current density profile. Quantitative models exist for each of these two criteria and are used to predict if a given pedestal pressure profile is stable to peeling–ballooning modes or KBMs. These models have sufficient quantitative accuracy for the conventional aspect ratio C-Mod and DIII-D devices that they have been combined into a single model, the EPED model [3], which successfully predicts the pedestal width and height in type-I ELMing discharges in these machines to within about 20% over a wide range of parameters. The EPED model provides a good basis for predicting the pedestal height in ITER. Significant progress was made to extend this capability towards the low aspect ratio NSTX machine; but due to challenges of modelling low aspect ratio devices, the width physics is not yet adequately modelled for good quantitative predictive capability.

Successfully optimizing the pedestal for multiple criteria in ITER and other future machines will require an improved understanding of individual density and temperature profiles.

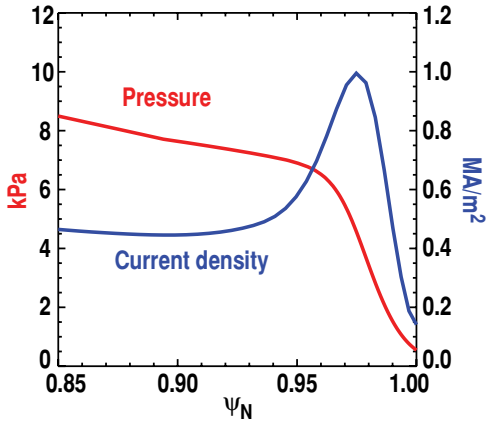

Figure 1. Profiles of edge current density (peaked at edge) and total plasma pressure for DIII-D discharge 144981 with total plasma current = 1.5 MA. The region of large pressure gradient ($\psi_N \sim 0.96$–1.0) drives a large bootstrap current.

A significant effort was made as part of the JRT to develop and compare theoretical models for these profiles to experimental data. These include models for neoclassical transport, paleoclassical and fuelling physics to explain the density pedestal, models for paleoclassical transport and electron temperature gradient (ETG) turbulence for the electron temperature profile and electromagnetic gyrokinetic models for fluctuation-driven transport in the pedestal. None of the examined models was ruled out as a possible contributor to pedestal structure, at least in some regimes. Rather, the results suggest that several processes may play a role in pedestal structure and integrated pedestal models will need to include multiple processes in a self-consistent way to make satisfactory predictions of detailed pedestal structure.

The outline for this paper is as follows: section 2 describes the theoretical and experimental work performed to understand the limits to the total pedestal pressure profile. Section 3 discusses the comparison of theoretical models to experimental data for temperature and density profiles. Section 4 provides a summary and conclusions.

2. Limits to pedestal pressure

A defining characteristic of an H-mode discharge is a pedestal in the edge pressure profile (figure 1) which is a region of steep pressure gradient just inboard of the last closed flux surface. Experiments have shown that higher pedestals in temperature or pressure are associated with higher total stored plasma energy, due both to increases of energy stored in the pedestal and due to improved core confinement [4–6]. Theory-based modelling shows that this effect is a logical consequence of the core transport being determined by critical gradient physics [7, 8]. Thus, the height of the pressure pedestal plays a major role in the performance of current tokamak devices and is predicted to have major impact on the performance of ITER. For instance, calculations based on the TGLF model predict that the fusion power in ITER will increase nearly as the square of the pedestal pressure [9]. Therefore, there is an important need to predict and to optimize the pedestal height in ITER.

The JRT research has added to a worldwide body of research that supports a picture of the physics processes that

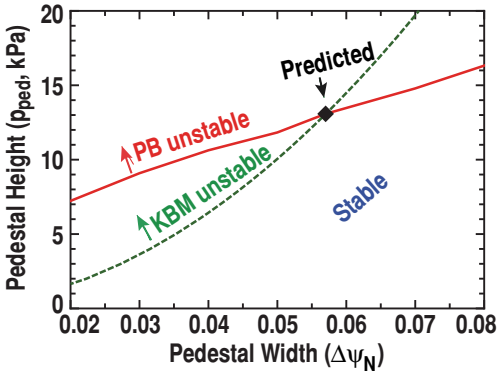

Figure 2. Example of peeling–ballooning and kinetic-ballooning constraints on pedestal pressure, predicted to limit the attainable pressure in a space of pedestal pressure height versus pedestal pressure width. For this model, height is defined as $2T_{e,ped}n_{e,ped}$, and width is the average of the T_e and n_e widths, where all parameters are evaluated with a tanh function. Allowed (stable) operating space is below both constraints. A type-I ELM is predicted to occur at the intersection of the two constraints. Calculation is for a DIII-D discharge.

provide upper limits on the evolution of the pedestal pressure profile [10, 11]. In this picture, the two primary physics elements determining the limits are the pressure profile itself and the pedestal current density profile, which has an important contribution from the bootstrap current, driven by pressure gradient. Global limits to the pedestal pressure profile are set by finite-n ideal peeling–ballooning modes. Smaller scale and more localized modes, KBMs, limit the local pressure gradient. The EPED model [3], which combines these processes, has successfully predicted pedestal width and height in existing machines. Figure 2 provides a schematic view in a space of pressure height and width of how the constraints limit the operating space, which is that region which is stable for both the global and more local modes. Several tests of the physics elements in the model have been performed in this research effort and these are discussed here.

The model was developed to predict the pedestal pressure (and width) obtained just prior to the onset of a type-I ELM. The model would need additional physics to describe most other H-mode regimes of operation, such as ELM-free regimes or type-III ELM regimes. Some other regimes might have physics that provide pressure limits at levels below the peeling–ballooning threshold. In these cases, the EPED model would not be expected to provide a calculation of the pedestal operating point. However, the global limits to the pressure set by peeling–ballooning modes are expected to apply to all regimes of H-mode operation in the sense that these regimes are not expected or known to operate at pressures above the peeling–ballooning threshold. There is some discussion of pressure limits for some ELM-free regimes in section 2.1.2; depending on the regime, the pedestal is observed to operate at or below the peeling–ballooning threshold. It is also possible that in some regimes of operation, some additional physics limits the local pressure gradient to levels below the kinetic-ballooning threshold. In those cases, the model would not be expected to apply either. Most of the experimental data presented here are obtained from type-I ELMing regimes, which is the appropriate regime for testing the model.

2.1. Global limits to pressure

2.1.1. Pedestal bootstrap current. Large pressure gradients in the pedestal drive an edge bootstrap current. This current plays an important role in the physics of peeling–ballooning modes and must be known accurately in order to compute the stability threshold. The magnetic shear, strongly modified by the bootstrap current, is also an important quantity in several pedestal transport models. The bootstrap current is computed from theoretical neoclassical models, such as the Sauter model [12] or the NCLASS model [13] for use in models of peeling–ballooning stability. Due to the important role of the bootstrap current, it is important that these theoretical models be validated, preferably against experiment. There have been some measurements of bootstrap current on DIII-D [14, 15] and MAST [16] and neoclassical models have been found to be in close agreement with these measurements in steady state.

In the JRT activity, there was significant work to benchmark new kinetic models for the bootstrap current against the simpler models in general use. This work was done with the XGC0 [17] code, the NEO [18] code and a global pedestal drift-kinetic code (denoted GPDKC here) [19]. All of these codes perform kinetic calculations in realistic geometry.

XGC0 is a full-f drift-kinetic particle code, which is equipped with a mass–momentum–energy conserving collision operator, and has been used to compute the edge bootstrap current in a realistic diverted magnetic field geometry with a self-consistent radial electric field [20, 21]. For pedestals in the weakly collisional banana-plateau regime (electron collisionality $\nu_{*e} \ll 1$), this code finds agreement with the Sauter model within several per cent, except for a thin layer, adjacent to the separatrix, with a width of about 1% of the minor radius. This agreement is found for C-Mod, DIII-D and NSTX. However, for pedestals in the plateau-collisional regime ($\nu_{*e} \geqslant 1$), the bootstrap current computed with XGC0 can differ by tens of per cent from the Sauter result. This effect is attributed to physics of the interactions between passing and trapped particles in the boundary layer. The sign of the difference with the Sauter result is dependent on aspect ratio. XGC0 computations for the low aspect ratio device NSTX predict a bootstrap current that is significantly larger than obtained from the Sauter model. In contrast, the XGC0 bootstrap current for the conventional aspect ratio DIII-D device at high collisionality is smaller than that from the Sauter model [20]. This aspect ratio effect is attributed to the much tighter spiralling of field lines on the high field side of a low aspect ratio device as compared to a conventional aspect ratio machine. An analytic model, based on the formulation of the Sauter model, has been developed to compute the XGC0 bootstrap current [20].

NEO is a δf drift-kinetic code that implements the fully linearized Fokker–Planck collision operator [18]. The code employs a sophisticated numerical algorithm that accurately treats the disparate velocity scales that arise in the case of multi-species plasmas and thus allows modelling of a plasma with an impurity species. Calculations with NEO including the full linearized Fokker–Planck collision operator and a carbon impurity find small but significant (∼10–20%) differences in the bootstrap current from that calculated in simplified models such as NCLASS or Sauter.

A new global pedestal drift-kinetic code (GPDKC) uses a continuum (Eulerian) framework and includes the exact linearized Fokker–Planck–Landau collision operator [19]. Non-local effects are incorporated in a numerically efficient manner, including both radial variation and strong poloidal variation, together with the pedestal radial electric field, E_r. The code uses a δf ordering that allows the ion density and electron temperature scale lengths r_n and r_{T_e} to be comparable to the ion poloidal gyroradius ρ_θ, while the ion temperature scale length r_{T_i} is assumed greater than r_n, as has been observed in several tokamaks. In scans over a wide range of collisionality, the Sauter bootstrap current formula is found to agree with results of this code within 10% at low collisionality, $\nu_{*e} < 0.5$, for DIII-D. However, the Sauter model can give a bootstrap current more than twice the value of the code when $\nu_{*e} \geqslant 4$. The discrepancy in the bootstrap current at high collisionality does not depend on finite-orbit-width or E_r effects, persisting even in the r_n, r_{T_e}, $r_{T_i} \gg \rho_\theta$ local limit employed by conventional neoclassical theory and codes. Thus, GPDKC and XGC0 provide qualitatively similar results for a conventional aspect ratio: the Sauter model agrees with these codes at sufficiently low collisionality but provides higher values of bootstrap current at sufficiently high collisionality.

A comparison of the predictions of the analytic Hirshman model [22], a new analytic model by Callen [23], the Sauter model and the analytic XGC0 model has been performed for representative DIII-D and NSTX discharges [24]. This comparison finds that the bootstrap current predictions of these models agree within about 10% for the DIII-D discharges but differ by more than a factor of two for NSTX. Variations with collisionality were not studied.

Taken together, the work described here indicates that the Sauter model is in good agreement with newer models, including the XGC0 and GPDKC models, for sufficiently low collisionalities. At higher collisionalities ($\nu_{*e} \geqslant 1$), the models can give significantly different results, with the differences being larger for the low aspect ratio of NSTX. These results provide increased confidence in the use of the Sauter model for calculations of bootstrap current at low collisionality, a common H-mode application, and indicate a need for caution in use of bootstrap current models at higher collisionality, particularly at low aspect ratio. Although there are large differences between some models for bootstrap current predictions at high collisionality, the uncertainty is not expected to have large effects on predictions of pedestal performance if the bootstrap current is relatively small compared to its collisionless value. An issue which may be of equal or greater importance for bootstrap current predictions is an improved characterization of pedestal impurities from the experimental side and an improved understanding of the impurity effects on bootstrap current on the theoretical side. The presence of impurities can have significant effects on the bootstrap current, certainly through changes of collisionality. Ultimately, though, given the importance of the bootstrap current in the pedestal physics, experimental measurements of the bootstrap current are needed to allow benchmarking of codes with high confidence. As noted previously, measurements of pedestal current density have been made on both DIII-D [14, 15] and MAST [16]. Significant improvements have been made to diagnostics on DIII-D as part of the JRT to measure the pedestal current density. These include upgrades to a lithium Zeeman spectroscopy/polarimetry system [15], which obtained data in FY12, now being analyzed.

2.1.2. Peeling–ballooning limits to pedestal pressure. Intermediate wavelength MHD instabilities driven by the sharp pressure and current gradients in the edge barrier ('peeling–ballooning' modes) have been proposed as a mechanism for driving ELMs and constraining the pedestal [25]. Models based on peeling–ballooning (PB) theory have been successful in predicting the observed boundary for instability to type-I ELMs within experimental uncertainties on a number of machines [11]. It has also been empirically observed that peeling–ballooning physics provides the ultimate limits to attainable pedestal pressure in the H-mode regime. That is, no machine has reported operating in the unstable region predicted by PB theory. As part of the JRT research, models of peeling–ballooning modes have been extended for applications to the compact, high-field C-Mod device and the low-field, low aspect ratio NSTX device. Peeling–ballooning stability analysis of type-I ELMing regimes and regimes in which ELMs were suppressed or not observed was performed on all three machines. The results support the premise that these models are able to quantitatively predict the ultimate limits to the pedestal pressure.

In the experimental studies reported here, a standard analysis methodology was adopted to process and compare data from C-Mod, DIII-D and NSTX. The analysis workflow was to: obtain measurements of pedestal T_e and n_e profiles from high resolution Thomson scattering systems [26–28]; obtain measurements of pedestal T_i and low-Z impurity density with high resolution charge exchange recombination spectroscopy when available [29–31]; obtain magnetic equilibria with the EFIT [32] code; use a set of python software tools to fit analytic functions to edge profile data [33]; generate 'kinetic' equilibria with the EFIT code where the pressure profile was constrained by experimental measurements and the edge bootstrap current was calculated from experimental measurements with the Sauter [12] model. For calculations of peeling–ballooning thresholds, a series of Grad–Shafranov equilibria were generated to map out a space of pedestal pressure gradient and current density by perturbing the pressure and current density profiles used to represent the actual experiment.

Type-I ELMy H-mode discharges on C-Mod, spanning a broad range of operational parameters, including plasma current (0.4–1 MA), toroidal magnetic field (3.5–8 T), and plasma shaping, were performed as part of this research [34]. Peeling–ballooning stability calculations have been made for a subset of these ELMy discharges, verifying proximity of the pedestal to the calculated stability boundary for medium-n modes. As an example, figure 3(*a*) shows that the experimental operating point for a C-Mod type-I ELMy discharge was within error bars of the computed threshold for the onset of PB modes, as calculated with the ELITE code [35]. Figure 3(*b*) shows analysis from a companion discharge in DIII-D, which was performed as a pedestal dimensionless parameter match to the C-Mod discharge. In the space of normalized edge current density versus normalized pressure

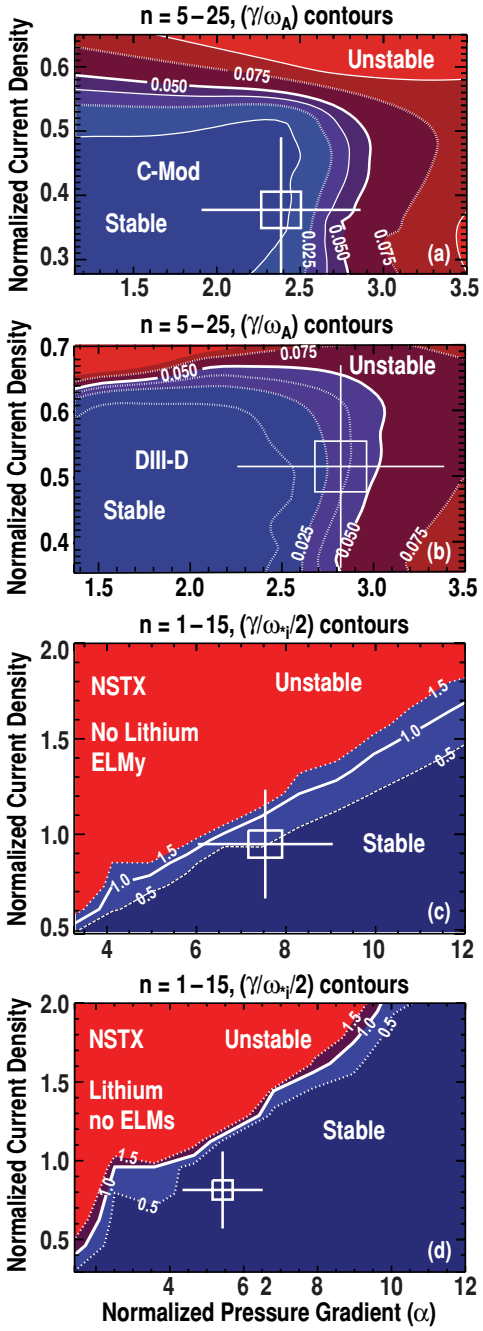

Figure 3. Stability limits for peeling–ballooning modes, as predicted with the ELITE code, for (*a*) ELMy discharge 1101214029 in C-Mod, (*b*) ELMy discharge 145716 in DIII-D, (*c*) ELMy discharge in NSTX, (*d*) discharge without ELMs in NSTX, obtained with lithium wall coatings. Normalized current density is the average pedestal current density divided by the average plasma current density. Normalized pressure gradient is the MHD α parameter, defined in [36]. Boxes are experimental operating points. In (*a*)–(*c*), these are points just before the onset of a type-I ELM. Thick solid contours show model criteria for instability thresholds.

gradient, the operating points and stability diagrams for the C-Mod and DIII-D discharges were very similar. In this comparison, the threshold for instability is obtained from the criterion $\gamma/\omega_\alpha > 0.05$, where ω_α is the Alfvén frequency and γ is the linear growth rate for the fastest growing peeling–ballooning mode. The calculated $n = 25$ mode structure is also found to be very similar for the equilibria from the two machines. This comparison used the instability threshold criterion $\gamma/\omega_\alpha > 0.05$ rather than the more common criterion $\gamma/(1/2\omega^*_{\rm pi}) > 1$, where $\omega^*_{\rm pi}$ is the ion diamagnetic drift frequency. The comparison was done in this way because diamagnetic effects can be strong in C-Mod pedestals and a more sophisticated diamagnetic model may be needed to accurately compute the instability threshold in C-Mod. The comparison of thresholds in terms of the Alfvén frequency is more direct since the code outputs the threshold in terms of this parameter. For DIII-D like conditions, the two criteria give similar results.

The NSTX device obtained a significant data set to document the effects on pedestal stability due to various thicknesses of lithium coatings on the walls of the machine [37]. Initial studies of edge stability with ELITE showed that ELMy discharges in this study were all near the kink/peeling boundary, far from the ballooning boundary; ELM-free discharges were in the stable operating space as computed by the model [38]. For these studies, the threshold condition for ELM onset was found to be approximately $\gamma/(1/2\omega^*_{\rm pi}) > 0.1$. This threshold was notably lower than the diamagnetic criterion typically used in DIII-D and other machines: $\gamma/(1/2\omega^*_{\rm pi}) > 1$ [3]. Subsequently, two improvements to the analysis have been identified which resolve this difference, as demonstrated in figure 3(*c*). This figure shows that for a type-I ELMing discharge, the NSTX operating point before an ELM was consistent with the usual threshold for instability. One change in the analysis was the use of the bootstrap current from the XGC0 model, which computes a significantly higher current than the Sauter model, used for the original stability calculations. The second and possibly more important change in the analysis was the inclusion of mode numbers down to $n = 1$ in the analysis, as opposed to a minimum $n = 5$, typically used for conventional aspect machines. This work has shown that the PB calculations are significantly more complex at low aspect ratio than at moderate aspect ratio. Thus, more work is needed to obtain a firmer understanding of the PB threshold at low aspect ratio.

Pedestals that clearly lie in the predicted unstable regions have not been observed in this work. However, all three machines observed good confinement regimes without ELMs that operated at or below the predicted PB threshold. Stability analysis of DIII-D discharges showed that the QH-mode regime operates near the PB threshold and the ELM-suppressed regimes obtained with the application of resonant magnetic perturbations lie below the limit [33]. ELM-free regimes in NSTX obtained with the application of lithium coatings operated below the PB limit (figure 3(*d*)) [38]. In C-Mod, discharges in the I-mode regime [39] exhibit H-mode like gradients in T_e, L-mode like gradients in n_e and operate well below the predicted PB limit [40]. Enhanced D_α (EDA) discharges [41] in C-Mod operate close to but below the PB threshold [40]. In summary, peeling–ballooning theory provides an upper limit to the attainable pedestal pressure in the experiments performed in these machines.

2.2. Limits to local pressure gradient

A model, based on nearly local KBMs, has been proposed to provide a second constraint on the pedestal pressure profile [3]. The hypothesis behind this model is that these modes turn on strongly when the pedestal pressure gradient reaches a critical value α_c. These modes are smaller in scale than peeling–ballooning modes and do not cause a collapse of the pedestal as an ELM does, but keep the pressure gradient clamped to near the KBM threshold value. For typical tokamak operation, this threshold value has a dependence on the current density given by $\alpha_c \sim 1/s^{1/2}$, where s is the local magnetic shear at the outboard plane. Thus, the pressure profile and current density profile are important physics elements in this model, as they are in the model for peeling–ballooning stability. Various tests of this model have been performed and are discussed below.

2.2.1. Pedestal width scaling. To leading order, the physics in the model implies that the pedestal width has the form $\Delta_{\psi_N} = \beta_{p,ped}^{1/2} G(\nu_*, \varepsilon, \ldots)$ where $\beta_{p,ped}$ is the pedestal beta poloidal and the function of G has a weak dependence on collisionality ν_*, aspect ratio ε and other dimensionless parameters [42] with a value of the order of 0.1. The width Δ_{ψ_N} in this scaling is defined as the average of the T_e and n_e widths, evaluated with fits of a tanh function to the pedestal profiles and is measured in normalized poloidal flux. The pressure required to evaluate $\beta_{p,ped}$ is obtained from $2T_{e,ped}n_{e,ped}$, where $T_{e,ped}$ and $n_{e,ped}$, are the pedestal values for T_e and n_e, as determined from fits with the tanh function.

Prior to the JRT, the equation for Δ_{ψ_N} was evaluated analytically with G being used as a constant obtained from experiment. A newer model, called the 'ballooning critical pedestal' (BCP) technique, has been developed to compute Δ_{ψ_N} [42] without the need for a free parameter. This model is based on the assumption that the KBM critical pedestal pressure gradient is well approximated by the critical gradient for the onset of infinite-n ideal ballooning modes. In practice, the BALOO code [43] is used to evaluate ideal ballooning stability in the pressure profile and the model width is taken as twice the width of the region whose pressure gradient is at or beyond the threshold for excitation of these modes. The width obtained from the numerical BCP technique is usually very close to the width obtained from the original analytic expression.

Systematic pedestal width measurements from all three machines have been obtained and used to test these models for pedestal width. Data for each of the machines were fit to this analytic width expression to obtain empirical values for G. For the moderate aspect ratio machines C-Mod [34] and DIII-D [3, 44], the best values of G are nearly identical, 0.088 and 0.076, respectively. For the low aspect ratio NSTX [45] device, the best value is 0.17. The BCP technique has also been used to derive best model values for c for the scaling expression $\Delta_{\psi_N} = c\beta_{p,ped}^{a}$ for the three machines, as illustrated in figure 4. In this work, a was fixed at 0.5 for C-Mod and DIII-D and at 0.8 for NSTX. The value of 0.5 is obtained from analytic approximations used in the original version of the EPED model [3] and later found to be consistent with the upgraded version of the model, using the BCP technique [42]. The value of 0.8, used for NSTX, is obtained from initial BCP

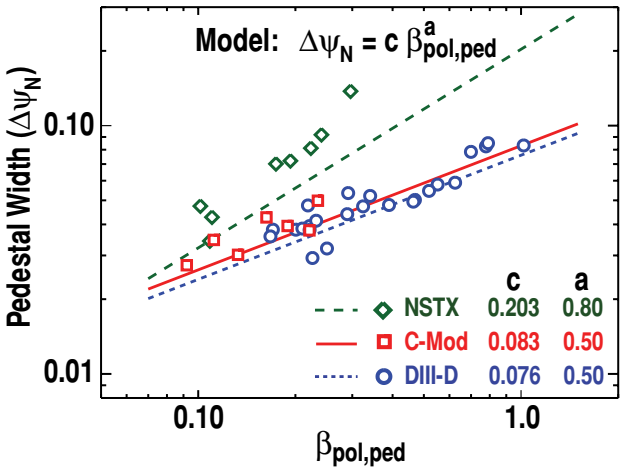

Figure 4. Pedestal width, defined as the average of the T_e and n_e widths versus pedestal beta-poloidal, where pressure is defined as $2T_{e,ped}n_{e,ped}$. Symbols show experimental measurements from C-Mod, DIII-D and NSTX. Lines show predictions of the BCP model, using the equation shown.

calculations that evaluate the dependence of pedestal width on aspect ratio. These calculations, which are very challenging at low aspect ratio, have not yet reached the aspect ratio of NSTX, and it is possible that improvements to the coefficient will be obtained in future work. Best values of c are 0.083 for C-Mod, 0.076 for DIII-D and 0.203 for NSTX. Figure 4 shows that the experimental width scaling for C-Mod and DIII-D lie along nearly the same trajectory, that the BCP technique for the KBM-based width provides a very good fit to C-Mod and DIII-D, that there is an aspect ratio dependence to the experimental widths with the NSTX widths being larger than those of the other two devices, and that the BCP partially but not totally captures this aspect ratio dependence. The BCP line for the NSTX data was obtained from application of the BCP model to a couple of experimental points and thus provides an average predicted trend over the existing experimental data, shown in the plot.

These results indicate that the same underlying physics controls the width of the pedestal and that it contains a significant dependence on aspect ratio. Models based on the assumption that KBM physics controls the width provide a very good description of measurements in the conventional aspect ratio machines C-Mod and DIII-D. These models capture much of the scaling in the low aspect NSTX device. KBM calculations are highly challenging at low aspect ratio and it is possible that further work will improve the agreement of the model with the data. Confidence in these scaling results, particularly in comparing the results from the machines, is aided by the fact that the same diagnostics, high resolution Thomson scattering systems [26–28], and the same profile fitting code [33] were used in obtaining and analyzing these data. Thus, possible systematic errors due to the use of different diagnostic measurements or different fitting codes are greatly reduced in these comparisons.

2.2.2. Temporal evolution of pressure gradient. The buildup of the pedestal between ELMs provides another test for hypotheses that KBMs limit the pedestal pressure gradient.

Previous studies on DIII-D [46, 47], AUG [48, 49] and MAST [50] have provided evidence that the pedestal pressure gradient rises to near its maximum level quickly after recovery from an ELM and then evolves slowly or is saturated until the onset of the next ELM. During the ELM cycle (recovery of one ELM to onset of the next ELM), the pedestal width, particularly for the density profile, has been observed to increase [46, 47, 50]. As illustrated in figure 5, similar new observations were made on NSTX [45] (figure 5(*a*)), C-Mod [40] (figure 5(*b*)) and DIII-D [51] (figure 5(*c*)) as part of this research. In particular, for ELM cycles during which time-resolved measurements could be made, the maximum pedestal pressure gradient is observed to come to saturation or near-saturation early in the ELM cycle with the pedestal observed to increase in width at nearly constant pressure gradient during the ELM cycle.

Given these observations, it is of interest to compare the pressure gradient evolution during the ELM cycle to the predictions for the KBM limits to the gradient. Previous measurements in a discharge with long ELM periods (∼100 ms) have shown that the pedestal width and height evolve along a trajectory as expected if KBM modes are limiting the pressure gradient [47]. New measurements, obtained with improved spatial resolution from an upgraded Thomson system on DIII-D [27], have confirmed these observations for a 1 MA discharge [51]. As shown in figure 6, good agreement of the constraint with the measured pedestal evolution is also observed in a scan of plasma current I_p where the current was varied from 0.5–1.5 MA. The constraint predicts the qualitative and quantitative trends of the pedestal evolution for all three currents with reasonable agreement with the measurements. In these discharges, the maximum pressure gradient varied by about a factor of 8. Agreement of the model with the data over this range of conditions is strong confirmation that the model is capturing the dominant trends in the data. In the context of this model, it is plausible that the pressure gradient could lie below the KBM limit under some conditions, possibly early in the ELM cycle immediately after an L–H transition. This is a topic of current research.

2.2.3. Search for KBMs in experiment. Improved confidence that KBMs limit the pressure gradient requires observation of KBM fluctuations in experiment and confirmation that they have the qualitative and quantitative characteristics predicted from simulations of these modes. Both experimental and simulation work have been performed to address these issues. High frequency coherent (HFC) modes [52], with the characteristics expected for KBMs, have been observed in some conditions in QH-mode discharges. The HFC modes turned on during an increase in the pedestal pressure, which then stopped rising. KBM-like features included a mode frequency of 0.2–0.3 times the ion diamagnetic frequency, a propagation direction in the ion diamagnetic direction in the plasma frame, a mode decorrelation rate exceeding the $E \times B$ shearing rate and a medium-n mode number (n ∼10–25). The intensity of broadband density turbulence has also been observed to increase rapidly after an ELM crash, as the pedestal pressure is increasing, and to saturate at about the same time as the pedestal pressure saturates [53]. These fluctuations also exhibited characteristics expected for KBMs, including propagating in the ion diamagnetic direction in the plasma frame and exhibiting a turbulence decorrelation rate that exceeds the equilibrium $E \times B$ shearing rate.

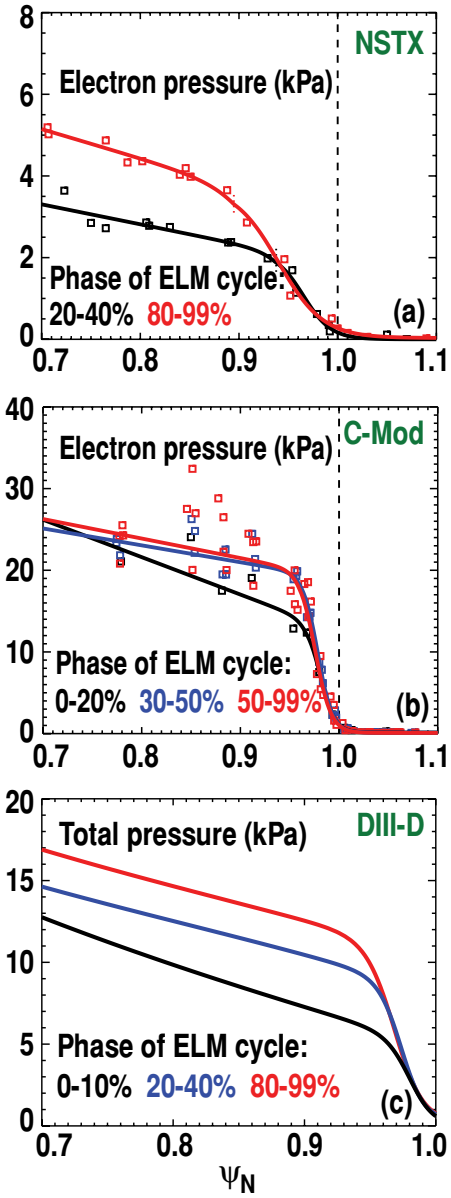

Figure 5. Evolution of pedestal pressure profiles from early in the ELM cycle to late in the ELM cycle for (*a*) NSTX, (*b*) C-Mod and (c) DIII-D. Electron pressure shown in (*a*) and (*b*); total pressure in (*c*). As used here, the ELM cycle starts at completion of an ELM crash and finishes at the next crash. Thus, the 50–99% or 80–99% phase represents pedestal conditions near the onset of an ELM.

The relation between density fluctuations and the evolution of the pedestal pressure gradient has also been examined in DIII-D in the ELM-free period after a transition to H-mode. These data were obtained with the heating power near the threshold power with the goal of maintaining the evolution of the pedestal as slow as possible to aid in making time-resolved measurements. Figure 7(*a*) shows D_α emission for a discharge in which the L–H transition occurred at about 4965 ms. After the end of a short phase of type-III ELMs that followed the transition, the intensity of long wavelength density fluctuations with poloidal wavenumber $k_\theta < 0.4\,\mathrm{cm}^{-1}$,

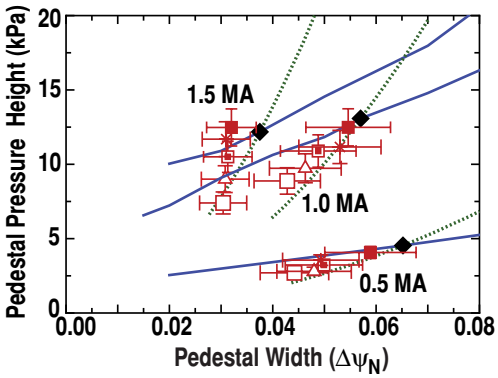

Figure 6. Theoretical limits on pedestal pressure width and height as set by peeling–ballooning constraints (solid curves) and kinetic-ballooning constraints (dashed curves) as computed for three different plasma currents in DIII-D. Solid diamonds are predicted operating points achieved at the onset of type-I ELM. Solid squares are measured operating points achieved just before the type-I ELM crash actually occurred. For each current, the data points show experimental progression of pedestal structure parameters during pedestal buildup between ELMs. The progression in time is from lowest height/width points to the points just before the ELM onset. Within error bars, the measured operating points follow the KBM constraint during pedestal buildup to the ELM crash.

measured with a beam emission spectroscopy (BES) diagnostic [54], dropped to a very low level, remained low for about 15–20 ms and then exhibited an abrupt turn-on of multi-harmonic coherent fluctuations at about 4990 ms (figure 7(*c*)). As shown by a profile of the intensity fluctuation level, these fluctuations were localized to the pedestal (figure 8). The electron pressure gradient, as measured with a high spatial resolution Thomson scattering system showed a rapid increase of more than an order of magnitude during the time when the density fluctuation level was low (figure 7(*b*)). Coincident with the turn-on of the coherent density fluctuations, the rate of rise of the electron pressure gradient decreased markedly, as would be expected if the fluctuations were increasing pedestal transport. Figure 7(*b*) also shows the critical pressure gradient for the onset of KBMs as predicted by the analytic model for the width of the pedestal related to the pedestal height. The critical threshold was significantly above the experimental value of the gradient in the L-mode. Early in the H-mode, the experimental gradient rose to and started to track the threshold. This data set is consistent with the idea that the fluctuations in the H-mode were signatures of KBMs and that the KBMs constrained the pressure gradient. Definitive proof for this assertion requires developments in theoretical models to show clearly that the observed fluctuations are those expected for KBMs.

2.2.4. Search for KBMs in simulation. Simulations with appropriate modelling codes are needed to determine if the simple assumptions of the EPED model regarding KBMs are correct. Such simulations have been performed for the low aspect ratio MAST spherical tokamak and the results support the main assumptions for the implementation of the KBM constraint in the EPED1.6 model [50]. Several modelling studies of KBM physics were performed as part of the JRT research [55–57]. The results provide some support for the presence of KBMs in the pedestal, but overall the results are not as consistent as in MAST.

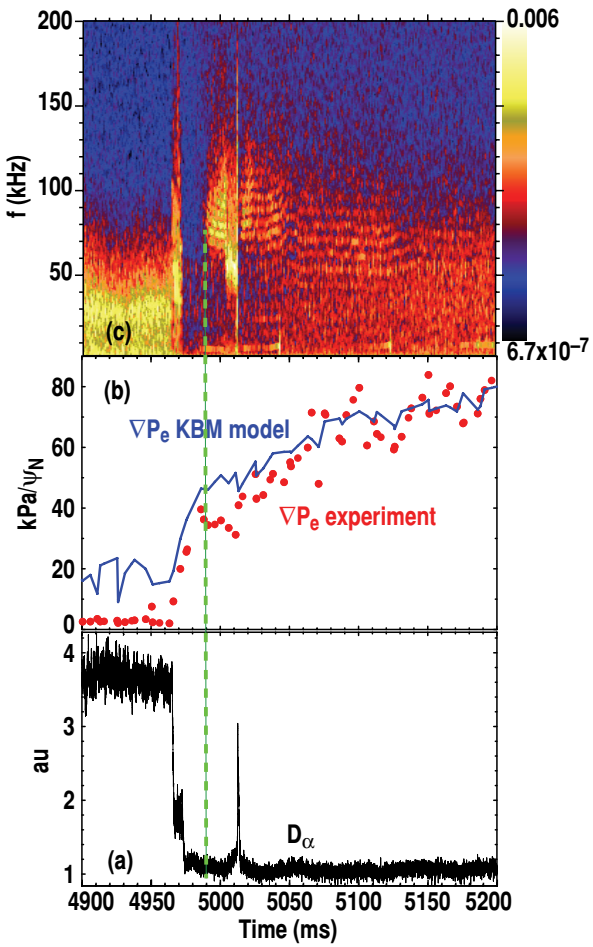

Figure 7. (*a*) Divertor D_α waveform; (*b*) solid circles show the time history of ∇P_e; the solid line shows theoretical threshold pressure gradient for the onset of KBM modes; (*c*) contour plot of intensity of density fluctuations in pedestal. After L–H transition at 4965 ms, ∇P_e rises rapidly, increasing by more than an order of magnitude until the onset of coherent density fluctuations, as denoted by the vertical dashed green line. After turn-on of fluctuations, the rate of rise of ∇P_e decreases markedly. In (*b*), ∇P_e in L-mode is well below the theoretical threshold for the onset of KBM modes. But, after L–H transition, ∇P_e rises to approximately the threshold within a few milliseconds and then tracks the threshold during the ELM-free phase of the discharge, during which density fluctuations continue. Data for DIII-D discharge 148698.

In the MAST studies, the pedestal evolution is similar to that described previously; the pressure gradient reached a near steady state early in the ELM cycle and the pedestal width expanded with time [50]. Calculations with the HELENA [58] code showed that much of the steep gradient region was unstable to ideal infinite-*n* ballooning modes and that the width of this region expanded as the pedestal grew in width. Linear, local simulations were performed with the GS2 gyrokinetic code [59] to examine the KBM stability. These modes were found to be the dominant instability in the pedestal and their existence closely followed the region that was unstable to infinite-*n* ideal ballooning modes.

Similar calculations [57] were performed for NSTX, a low aspect ratio machine as is MAST. In contrast to the MAST results, most of the pedestal was found to be in the second stable regime for ideal, infinite-*n* ballooning modes. Linear, local

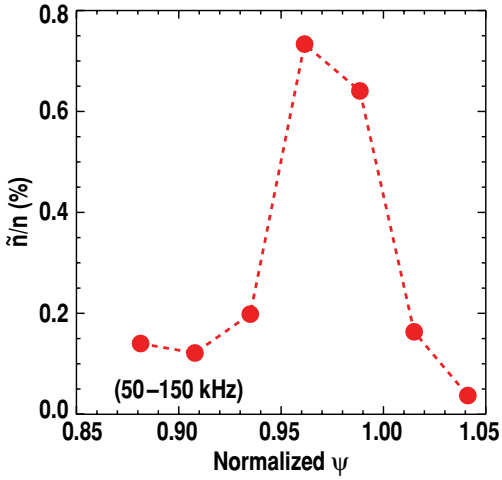

Figure 8. Amplitude of low-k density fluctuations normalized to line-averaged density as a function of ψ_N, measured with a BES system for DIII-D discharge 148698 at 5030 ms. Density fluctuations are localized to the pedestal.

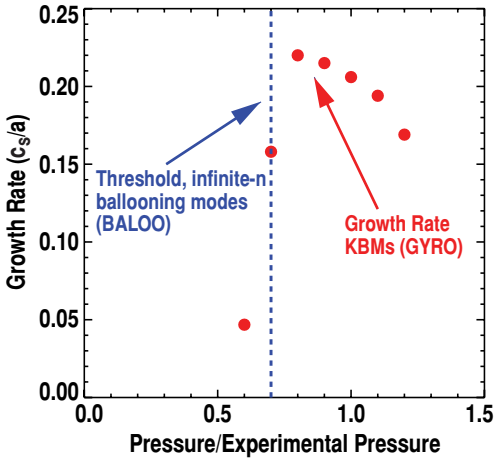

Figure 9. Solid circles are the linear growth rate for KBM (in units of ion sound speed over minor radius) as a function of pedestal pressure normalized to the experimental pressure, as computed with GYRO. KBM mode turns on at about 60% of the experimental pressure. The vertical dashed line shows the threshold for the onset of the infinite-n ideal ballooning mode, as computed with BALOO. All calculations performed with bootstrap current reduced below the experimental value to avoid peeling–ballooning modes in simulations. Analysis is for DIII-D discharge 131997.

calculations were performed with the GS2 code to examine the stability of KBMs over a range of magnetic shear and pressure gradient. The growth rates were found to be maximum near the first stability limit for ideal ballooning modes and to decrease as the pressure gradient was increased towards second stability for ideal ballooning modes. Similar to the MAST case, the region of instability for KBMs corresponded closely to that for ideal ballooning modes. However, these results do not support the idea that KBMs limit the pressure gradient since most of the pedestal was in the second stable region and the growth rates are predicted to decrease significantly for the increased pressure gradients of the second stable region. A future step in this analysis will be to determine if the inclusion of non-local effects would change the stability picture so that KBMs would be predicted to be the dominant modes in the pedestal [57].

Linear, local simulations were performed with the eigenvalue solver of the GYRO code [60] on a DIII-D discharge to study the stability properties of KBMs in the pedestal [55]. A major goal of these studies was to determine if the threshold for KBMs was approximately the same as the threshold for ideal infinite-n ballooning modes. Because the experimental data set represented conditions near the threshold for an ELM, the bootstrap current was artificially reduced in the analysis (to about half of its experimental value) to ensure that peeling–ballooning modes were stable in the simulations. A scan of pressure gradient from 50% to 120% of the experimental value was performed and similar thresholds were found for the onset of the kinetic ballooning and ideal ballooning modes. As shown in figure 9, onset of ideal modes, computed with BALOO, was at about 70% of the experimental pressure and the threshold for KBMs, computed with GYRO, was at a pressure of about 60% of the experimental pressure. In this respect, the results are consistent with NSTX and MAST in that the two modes have approximately the same threshold. But, the KBMs were found to be subdominant and an unnamed group of drift waves were predicted to have significantly higher growth rates. The use of the GYRO eigensolver was necessary for finding the KBM, given that it was not the fastest growing mode. Important future analysis would be to perform calculations with the full plasma current and to extend the calculations to include non-local effects.

Global calculations were performed [56] for two DIII-D discharges with the GEM electromagnetic gyrokinetic code [61]. The current density and pressure gradient in these discharges were initially taken as the experimental values, which were obtained by standard analysis shortly before the onset of a type-I ELM. In both cases, the strongest growing mode was an intermediate-n mode, a kinetic version of the peeling–ballooning mode, and was called a kinetic peeling–ballooning mode (KPBM). The relation between this mode and the ELM instability was not examined. However, in a second study, the q-profiles were artificially flattened in a small region around the point of maximum pressure gradient so that the magnetic shear was locally reduced to zero. These conditions stabilized the KPBM and slightly destabilized the KBM so that it was found to be the dominant mode in both discharges. These results suggest that global simulations may be important to properly study the KBM but they also point to the need to measure the current density or q profile or to at least develop an improved understanding of the uncertainties in existing reconstructions.

From these studies, it is clear that the role of KBMs is not fully established by code modelling and more work is needed. Several of these studies do provide evidence that the threshold for KBMs is approximately the same as for infinite-n modes. The existence of KBMs in a pedestal that is second stable to infinite-n modes is problematic and needs to be resolved. Global simulations may be part of the solution. The role of uncertainties of experimental measurements in these studies needs to be assessed and there is a clear need for measurements of the pedestal current density or q profile.

2.3. Tests of EPED model for pedestal height and width

The EPED model [3, 42] combines models of the constraints for both PB physics and KBM physics, discussed in the

previous sections, to simultaneously predict pedestal width and pedestal height (for pressure) for type-I ELMing discharges. The EPED model is depicted in figure 2, which shows the two constraints between height and width. The predicted operating point for the pedestal at the onset of an ELM is that point where the two constraints cross, i.e. where they are both active. As noted elsewhere [3, 42], the constraints for the two models are developed from a series of model profiles and equilibria which are developed from eight scalar input parameters: the toroidal field B_T, the plasma current I_p, the geometric major radius R, the minor radius a, triangularity δ, elongation κ, pedestal electron density $n_{e,ped}$ and $\beta_{N,global}$, the global normalized Troyon β. The first six parameters can be considered machine control parameters. If the final two parameters, $n_{e,ped}$ and $\beta_{N,global}$ can be achieved in an experiment, the EPED model can be used to predict the pedestal height and width either before or after an experiment. This model has previously been applied to data from a number of machines and found to provide a good prediction of pedestal height in these devices [10]. For the JRT work, significant advances were made in the model and new data sets from C-Mod and DIII-D provided tests of the model in new parameter ranges, as will be discussed below.

For the JRT research, the EPED model was upgraded (to version 1.6) to use the BCP model (section 2.2.1) to compute the constraint for KBM physics. The use of the BCP model does not produce significant differences from the original version of the model (version 1). However, EPED1.6 also contains an update to the diamagnetic stabilization criterion used to determine the threshold for the onset of PB modes [42]. This updated criterion is important for modelling high-field devices, such as C-Mod, in which diamagnetic effects can be quite strong in the pedestal.

The EPED 1.6 model has been tested against data from C-Mod and DIII-D and found to provide good predictions of pedestal height. Figure 10(*a*) shows results from application of the model to a number of recent discharges from C-Mod [34] and DIII-D [51] in which new data significantly extend the range for model testing. Data from C-Mod extended the maximum pedestal pressure by about a factor of two over previous tests of the EPED model. In the new data set, the measured pedestal pressure varies by a factor of about 20 and the quantitative agreement of the predictions with these measurements is typically within 20% or better. In addition, new data from DIII-D have significantly increased the data set of measured large widths in the range 0.06–0.08 in units of normalized poloidal flux of ψ_N, as shown in figure 10(*b*). These data are well matched by the EPED model.

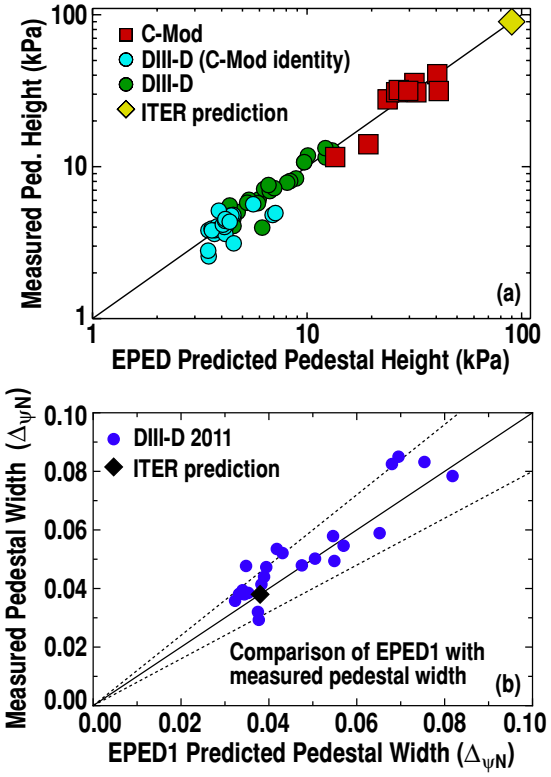

Figure 10. (*a*) Measured pedestal pressure height ($2n_eT_e$) versus predicted height from the EPED model for C-Mod and DIII-D experimental data from 2011. The solid line is the unity line. Also shown is the prediction for pedestal pressure in the ITER baseline scenario. (b) Measured pedestal width (average of n_e and $T_e$widths) versus predicted width for DIII-D. The solid line is the unity line; upper and lower lines are ±20%. Also shown is the prediction for pedestal width in the ITER baseline scenario.

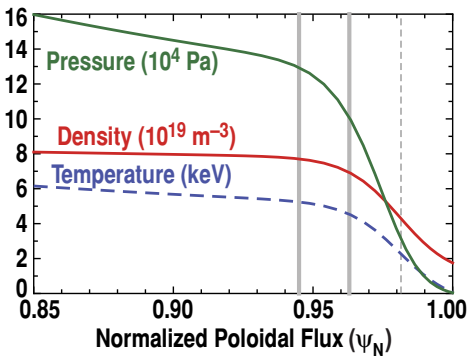

Figure 11. Pedestal density, temperature ($T_e = T_i$) and pressure profiles for the ITER baseline scenario, as predicted with the EPED model.

2.4. Implications for ITER

The success of the EPED model in predicting pedestal structure over a wide range of parameters in existing machines provides a good basis for using the model to predict pedestal structure in ITER and predictions for the height and width of the pedestal in the ITER baseline scenario are shown in figure 10(*a*). The pedestal height is an extrapolation of a factor of 3 from the existing dataset, which spans more than an order of magnitude, and the predicted normalized pedestal width lies well within the existing data set.

Model profiles for the simulation of the ITER baseline scenario [42] are shown in figure 11. For an assumed $n_{e,ped} \sim 7 \times 10^{19}$ m^{-3}, the pedestal height is predicted to have $\beta_{N,ped} \sim 0.6$ and the width to be $\Delta_{\psi_N} \sim 0.04$ (~4.4 cm). These conditions imply a $T_{i,ped}$ of about 4.5 keV. The implications for these pedestal conditions for the ITER fusion performance depend on the core transport model used in simulations. However, this modelled temperature is in the range needed to achieve fusion $Q = 10$, as implied by several transport models [1].

The EPED model has been used to perform optimization studies for the ITER pedestal. Given that the shape of ITER

is established and has little flexibility, optimization studies predict that higher pedestal densities would provide a route to higher pedestal pressure [62]. This effect originates from the prediction that the ITER pedestal will be limited by the peeling boundary of PB modes. Thus, increasing the density at a given pressure increases the collisionality, which decreases the bootstrap current at a given pressure, which provides a stability boundary that increases with density. This effect does have a limit; at sufficiently high density, the pedestal is predicted to be limited by the ballooning side of the PB curve and the pressure is expected to decrease with increasing density. For the ITER baseline scenario, the highest pedestal pressure is predicted at $n_{\mathrm{ped}} \sim 13 \times 10^{19}\,\mathrm{m}^{-3}$ [62].

3. Studies of transport processes for individual profiles

The thesis of the preceding section is that there now exists a good framework for understanding the limits to the pedestal pressure profile. In order to fully simulate tokamak performance and to optimize future machines, it is necessary to have a much deeper understanding of the physics of temperature and density profiles. This is true even in the context of the EPED model, which takes the global beta and the pedestal density as given plasma parameters. However, it cannot be known if these parameters can be obtained in future machines unless a better understanding exists of how profiles respond to sources of heat and particles. An improved understanding of the physics of individual profiles is needed for a number of other reasons, such as predicting the dynamic buildup of pedestal density and temperature in response to given sources, predicting the development of the bootstrap current, which is strongly affected by the evolution of the pedestal density and temperature profiles and knowing how effective various fuelling schemes will be in building up the pedestal density. As part of the JRT work, research was done on a number of physics processes that are proposed to play a role in controlling temperature or density profiles. This work is briefly summarized here.

3.1. Neoclassical transport

The XGC0 [17] code has been used to simulate the density pedestal buildup and the model includes combined effects of neoclassical particle transport, due to ion collisions, and neutral fuelling. The code qualitatively reproduces several features of the experiments, including the steep density gradients observed in the H-mode pedestal. Quantitative comparisons to data from C-Mod and DIII-D show that some anomalous particle transport is required in addition to neoclassical transport to match the experimental density profiles [63, 64].

An example comparison is shown in figure 12(*a*), which shows that the density profile computed from the neoclassical model is shifted outwards relative to the experimental electron density profile. In this calculation, the particle source is a combination of the beam particle source as well as the wall source. The wall source is adjusted to be comparable to the source computed with the ONETWO 1.5D transport code [65], but sensitivity studies show that the result is not sensitive to

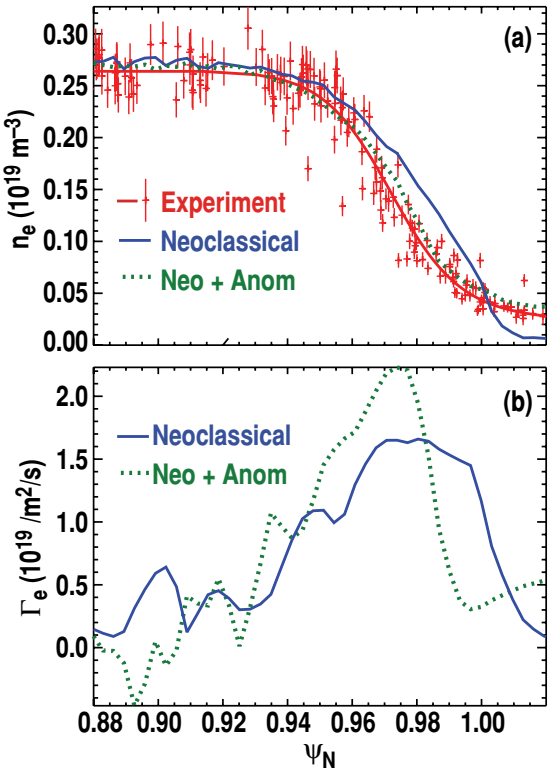

Figure 12. (*a*) Comparison of XGC0 model density profiles to the experimental density profile for DIII-D discharge 145716. Experimental n_e values (crosses), fit to expermental data (lighter solid line), modelled density profile with neoclassical transport (dark solid line), modelled density profile with neoclassical plus anomalous transport (dotted line). (*b*) Comparison of particle fluxes from the XGC0 neoclassical models with and without anomalous transport included.

significant changes of the wall source used in XGC0. As shown in figure 12(*a*), with the addition of anomalous particle diffusion to the neoclassical model the XGC0 calculation nearly matches the experimental density profile. Particle fluxes for the two XGC0 models are shown in figure 12(*b*), which indicates that only minor additional anomalous flux is needed for XGC0 to match the experimental density profile. These results suggest that neoclassical transport may be important in the density pedestal. Studies of the model under a wider variety of conditions would be helpful to benchmark the model.

3.2. Paleoclassical transport

Paleoclassical theory predicts that diffusion of poloidal magnetic flux causes radial transport of particles and energy [66]. The fundamental paleoclassical parameter is the poloidal magnetic flux diffusivity $D_\eta \sim T_e^{-3/2}$. Due to the rapid fall-off of T_e in the pedestal, D_η increases with radius in the pedestal and paleoclassical transport has been proposed to be the dominant source of transport in the pedestal. Moreover, an analytic model for T_e and n_e profiles resulting from paleoclassical transport has been developed for pedestal conditions [67]. Predictions of this model have been compared to experimental data in both NSTX and DIII-D.

Predictions of the model have been compared to electron density n_e and temperature T_e profiles obtained before and

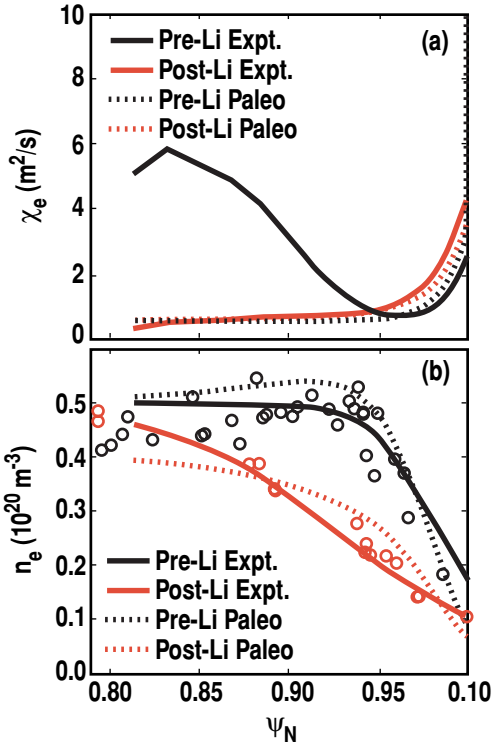

Figure 13. Experimental and paleoclassical values of (*a*) χ_{eff} and (*b*) n_e profile for NSTX discharges without lithium and with lithium. (Reprinted with permission from [37]. Copyright 2011 by the American Institute of Physics.)

after the application of lithium coatings in NSTX [37]. In this experiment, increasing lithium coatings on the wall of the vessel caused a profound change in the n_e profile, whose gradient was reduced and width increased with the addition of lithium. The pedestal T_e profile was not significantly changed with the coatings. The model made good quantitative predictions of the pedestal electron thermal diffusivity χ_e and of the shape of the pedestal density profile in NSTX discharges before and after lithium injection (figure 13). The model captured an increase of χ_e and a significant broadening of the n_e profile with the application of lithium.

The model has been evaluated for a large set of data in DIII-D covering a wide parameter range, including data from all pedestal experiments performed in 2011 [68]. Over this set of data, the average electron temperature gradient and the average electron density are predicted to be 1.7 ± 1.1 and 2.1 ± 0.7, respectively, times the experimental values. These comparisons were performed at the location of the steepest T_e gradient in the pedestal. Thus, the model predicts the minimum observed electron transport for many cases. In other cases, additional electron thermal transport or particle transport must be invoked to explain the results. If this is a correct model for pedestal transport, it is important to understand under what conditions the model applies. For this purpose, the ratio of the model to experimental temperature gradient was examined for several parameters [68]. The ratio tended to be close to unity for high confinement times, as measured from the ITER98y2 scaling [69], at lower values of global beta poloidal and at low pedestal T_e. At this time, it is not clear if one of these correlations captures an underlying physics trend. Comparisons of the model to data have also been done during various parts of an ELM cycle. These comparisons have been performed to examine the idea that paleoclassical transport might be the dominant transport early in the ELM cycle and that fluctuation-driven transport might turn on and dominate later in the cycle. An example of such comparisons is shown in figure 14, which shows comparisons of experimental values versus model predictions for n_e, ∇n_e, T_e and ∇T_e during ELM cycles from four discharges at three different currents (0.5, 1.0 and 1.5 MA). There is agreement of the temperature quantities for all cases except the lowest current case, which corresponds to the highest beta-poloidal in the study. For the higher currents, there is no sign of the model starting to under-predict late in the ELM cycle.

In summary, the paleoclassical model makes good predictions of the observed electron thermal transport under some conditions and under-predicts the observed transport in other conditions. Thus, the model represents the minimum amount of observed transport in these studies. For some conditions, additional transport mechanisms are required to explain the observations.

3.3. Fluctuation-driven transport—modelling

While fluctuation-driven transport is often invoked as a likely source of transport in the pedestal, modelling the relevant physics processes has proven to be very challenging. Some of the reasons include the need to model small spatial scales over which parameters change rapidly, the need to accurately account for plasma geometry and the need to account for kinetic effects in ions and electrons. There are also concerns about whether expansions used in existing fluid and gyrokinetic codes, which are logical tools for study of fluctuations in the pedestal, are valid for pedestal conditions. Despite these problems, there was a significant effort during the JRT to apply modelling tools to study fluctuations in the pedestal. The primary efforts were to perform linear simulations in order to obtain an idea of what modes might be unstable in the pedestal.

3.3.1. Electromagnetic gyrokinetic benchmarking. A benchmarking exercise was performed to compare electromagnetic gyrokinetic codes under pedestal conditions [55]. This comparison was performed between GEM [61], GYRO [60] and HD7 [70] with the DIII-D data discussed in section 2.2.4 as input. One of the major results was that each code has its own scheme for modelling the magnetic equilibrium and the details of how plasma geometry is modelled play a significant role in setting the growth rate in and near the pedestal. When it was possible to compare two codes with the same geometrical model, reasonable agreement was found between the codes when computing the growth rates and frequencies of the fastest growing linear modes. When GEM's shaping scheme was implemented in GYRO with calculations performed at $\psi_N = 0.9$ and 0.95, the growth rates from GEM and GYRO were nearly equal and the real frequencies agreed within a factor of two or less for modes with normalized wavenumbers $k_\theta \rho_s = 0.2$–0.8, where ρ_s is the ion Larmor radius. This range of wavenumbers corresponds to the longest wavelength and most dangerous modes expected to be present in the pedestal. When the circular geometry of HD7 was implemented in GYRO, the agreement between growth rates and real frequencies from HD7 and

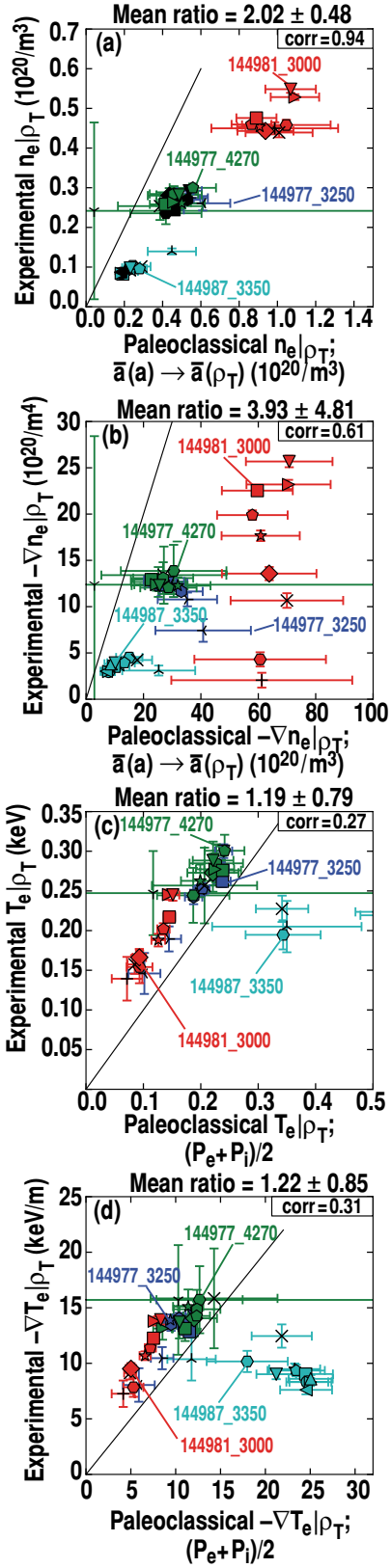

Figure 14. Comparisons of experiment to predictions from the paleoclassical model for (*a*) n_e, (*b*) ∇n_e, (*c*) T_e and (*d*) ∇T_e. All quantities evaluated at the steepest part of the T_e pedestal. Data shown for three different currents: DIII-D discharges 144977 (1.0 MA), 144891 (1.5 MA), and 144987 (0.5 MA). For each data set, points are obtained during evolution of an ELM cycle with measured parameters trending upwards with time.

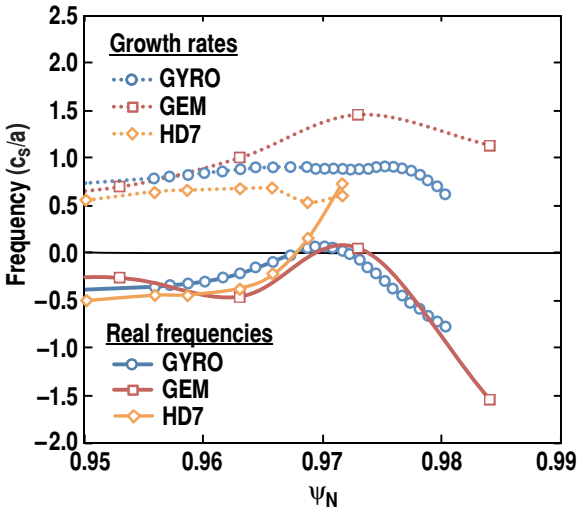

Figure 15. Spatial profiles of linear growth rates and real frequncies for most unstable modes at $k_\theta \rho_s = 0.25$, as calculated with three different gyrokinetic codes (GYRO, GEM, HD7). Each code is run with its native plasma equilibrium model. Simulations are for DIII-D discharge 131997.

GYRO was within 20% for the same parameter scan. In order to examine the importance of geometry in gyrokinetic modelling, a comparison of all three codes was performed, where the native geometry of each code was used in its calculations. A radial scan of frequencies was performed at $k_\theta \rho_s = 0.25$, the approximate normalized wavenumber where KBMs are expected. Figure 15 shows that qualitatively the results are similar for the three codes except that HD7 finds no unstable modes beyond $\psi_N \sim 0.97$. The frequencies from GYRO and GEM agree to within a factor of 2, even in the steep gradient region at $\psi_N > 0.97$. Differences between the three codes are likely due primarily to differences in how the codes implement plasma geometry [55]. GEM used a Miller [71] representation of the geometry, GYRO used a generalization of Miller geometry that includes squareness and elevation [72] and HD-7 used an $(s - \alpha)$ geometry consisting of toroidal circular flux surfaces with Shafranov shifts [73].

3.3.2. Unstable modes. The gyrokinetic modelling of a DIII-D pedestal, discussed above, has provided some results on what modes might be unstable on top of the pedestal and in the pedestal. On the pedestal top, GYRO found the ion temperature gradient (ITG) modes to be the most unstable modes for $k_\theta \rho_s < 1.5$ and that this transitioned to microtearing (MT) modes for $k_\theta \rho_s > 1.5$ [55]. In NSTX, calculations with GS2 predicted that MT modes were unstable in discharges without lithium and that these modes were stabilized and transitioned into trapped electron modes (TEM) with the application of lithium [57]. In the steep gradient region of DIII-D, GYRO found two unnamed modes competing for dominance for $k_\theta \rho_s = 0.1$–0.8 [55]. The wavefunctions for these modes were found to be extended in ballooning angle, to be peaked off the outboard midplane and to have fine radial scale lengths. The modes have twisting parity, with a small electromagnetic component. They are not observed in electrostatic simulations. In NSTX, ETG modes were found to be unstable in the steep gradient region; these modes were

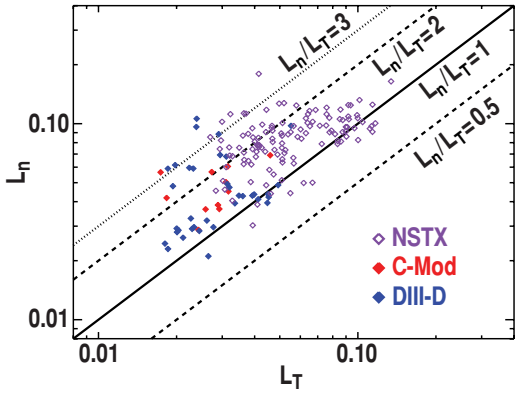

Figure 16. Scale length for electron density L_{n_e} versus scale length for electron temperature L_{T_e} for NSTX, C-Mod and DIII-D. Scale lengths expressed in terms of Δ_{ψ_N} and data measured at the steepest part of the electron pressure profile. Straight lines are lines of constant $\eta_e = L_{n_e}/L_{T_e}$.

more unstable in the discharges with lithium-coated walls [57]. The findings are more complicated than can be fully described here. The interested reader is referred to the references for more detail. These results show that the steep gradients of the pedestal can drive a host of instabilities. More work is needed to determine if there is a unified picture of which modes are unstable and what role, if any, these modes play in controlling the pedestal structure.

EDA discharges in C-Mod [40] have been modelled with the BOUT++ code [74, 75]. This work finds that unstable modes exist in the EDA pedestal when resistivity and ∇P are high. These predictions are consistent with experimental diagnosis of the quasi-coherent mode (QCM), which appears at high collisionality and high ∇P. A possible interpretation of the QCM is that it is a resistive analogue of the KBM and that it limits pedestal gradients in EDA discharges.

3.4. ETG turbulence

Small scale turbulence due to ETG modes has been proposed as a process to drive electron thermal transport in the steep pedestal [76]. Modelling of ETG modes with the GENE code [77] has predicted levels of electron thermal transport comparable to the measured transport in AUG [76]. Experiments have shown some qualitative and quantitative features expected for ETG modes. In particular, values of $\eta_e = L_{n_e}/L_{T_e}$, where L_{n_e} and L_{T_e} are the n_e and T_e scale lengths, have been measured to be in the range where these modes are expected to be excited. An example is shown in figure 16, which is a plot of L_{n_e} versus L_{T_e} for data obtained from C-Mod, DIII-D and NSTX. These values, evaluated at the steepest part of the electron pressure gradient, are mostly in the range of 1–3. Simulations with the GENE code predict that an η_e value of about 1.2 is the threshold for the onset of ETG turbulence [76]. Thus, essentially all of the pedestals represented by figure 16 are predicted to have ETG turbulence.

Studies were performed in DIII-D where strong electron heating, particularly from electron cyclotron heating (ECH), was applied to determine if the pedestal ∇T_e showed evidence of reaching a 'critical gradient' beyond which it would not evolve much, as would be expected for sufficiently strong

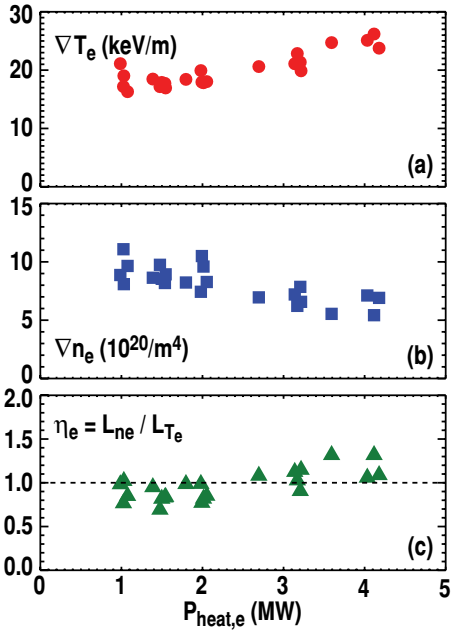

Figure 17. Variations of pedestal (*a*) ∇T_e, (*b*) ∇n_e and (*c*) η_e with electron power flow into the pedestal in the power scan in DIII-D. Heating power is a combination of beam power into the electrons and ECH power, deposited on top of the pedestal.

ETG turbulence. Most of the power was applied with ECH just inboard of the pedestal top; thus, much of this power was expected to flow directly through the electrons into the pedestal. Figure 17 illustrates that as the power into the electrons was increased by about a factor of 4, the pedestal ∇T_e increased by about 50%, the density gradient dropped by about 30% and η_e was near unity but increased slightly during the scan. These results could be consistent with the presence of ETG turbulence; if present, it was not so strong as to completely clamp the electron temperature.

As part of this experiment, a high-k backscattering system [78] was used to measure density fluctuations at small spatial scales, $k_\theta = 35\,\mathrm{cm}^{-1}$, where signatures of ETG turbulence would be expected. The relative density fluctuation level showed a weak decrease with increased heating power (figure 18). This trend is opposite to simple expectations of ETG modes increasing in magnitude with increased heating power. However, the dominant effect of increased power on ETG modes should be observed in the electron temperature fluctuations, which were not measured, and the density fluctuations might not show much effect from increased power. An important systematic issue is that the spatial resolution of the instrument was several centimeters; this is wider than the pedestal and thus the exact localization of the fluctuations is not known. Further interpretation of these results requires detailed non-linear modelling of ETG turbulence and of the predicted signals for the high-k scattering system.

The lithium experiment on NSTX was also used to look for evidence that ETG turbulence affected the pedestal structure [37]. In this experiment, the T_e profile was observed to be quite stiff in the pedestal, for $\psi_N > 0.95$, when the lithium coating was applied, even though the $n_e$gradient in the same region was reduced significantly (by ~50% or

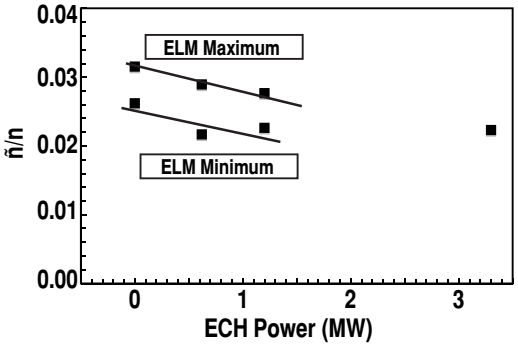

Figure 18. RMS intensity of density fluctuations normalized to line-averaged density from high-k backscattering measurement as a function of ECH heating power in DIII-D. Fluctuations were measured at a wavenumber of 35 cm^{-1} and originated from the outer 10–15 cm of the plasma edge. In addition to the ECH power shown, 2.3 MW of NBI power was applied in all conditions; total power varied from 2.3 to 5.6 MW. Data are shown early in the ELM cycle ('ELM minimum') and late in the ELM cycle ('ELM maximum').

more). Thus, η_e in the T_e pedestal was larger with lithium and would be expected to be more unstable to ETG modes. High-k scattering measurements showed the existence of fluctuations in the wavenumber range expected for electron scale turbulence. Reductions of high-k density fluctuations were observed when lithium was applied. However, it is difficult to definitively correlate the observed improvements of confinement with lithium with these reductions, because reductions in fluctuations at longer wavelengths were also observed with the application of lithium.

Simulations have been performed with the GS2 code to assess the linear stability of ETG modes in these NSTX discharges [57]. These show that ETG modes were unstable in discharges with and without lithium for the region $\psi_N > 0.95$. The growth rate was larger in the discharges with lithium, presumably because the density gradient was reduced and η_e was larger as compared to the pre-lithium discharges. Thus, ETG turbulence is a candidate for transport in the pedestal, particularly in the discharges with lithium.

In summary, the data of all three machines show qualitative and quantitative features expected for ETG turbulence in the pedestal. So far, though, there is no clear measurement of the amount of transport driven by ETG modes and thus it cannot be definitively said that these modes play an important role in pedestal structure. Progress in this direction requires non-linear simulations of ETG turbulence to compute transport levels and turbulence characteristics for comparison with experiments.

3.5. Neutral fuelling versus pinch

Fuelling of the pedestal by neutral deuterium atoms has been proposed as a mechanism for controlling the shape of the electron density pedestal, particularly its width [79]. An alternative hypothesis is that plasma transport, such as a particle pinch, plays the dominant role in controlling the structure of the density pedestal. As used here, the term 'pinch' implies a transport process that provides an inward particle flux. These two processes have potentially very different implications for ITER. Edge modelling for ITER has predicted that the scrape-off layer will be opaque to neutral penetration and raises significant uncertainties about fuelling requirements for ITER [80]. If there is a significant inward particle pinch in the pedestal, these concerns would be greatly reduced.

At least two modelling activities support the hypothesis that a pinch is important: (1) analysis of NSTX [37] data with the paleoclassical model in which a pinch is part of the transport physics and (2) analysis of DIII-D data with a model that combines constraints set by particle and momentum balance [81, 82]. The paleoclassical transport model for density has nearly balancing inward and outward forces on the particles, with the result that the actual shape of the particle source has little effect on the predicted density profile [67]. As reported in section 3.2, the paleoclassical model was successful in modelling the shapes of two very different density profiles obtained in NSTX, with and without the application of lithium coatings (figure 13).

A model, combining constraints of particle and momentum balance, has been developed for the interpretation of experimental data [81, 82]. This model determines that the main ion pressure profile must satisfy the relation $-(\partial p/\partial r)/p = (V_r - V_r^{\rm pinch})/D$, where p is ion pressure, r is the radial coordinate, D is a generalized 'diffusion coefficient', V_r is the radial ion velocity from particle balance, and $V_r^{\rm pinch}$ is a generalized 'pinch velocity' associated with the radial electric field, $V \times B$ forces and momentum input. The full definitions for D and $V_r^{\rm pinch}$ can be found elsewhere [81, 82]. In the interpretation of experimental data, this relation is solved for the ion pressure p and an experimental profile of the ion temperature is utilized to compute the density profile, implied by these constraints. An example of V_r and $V_r^{\rm pinch}$ computed from this model is shown in figure 19(a) and the inferred density profile closely matches the measured electron density profile, as shown by the example in figure 19(b). As shown in figure 19(a), the inward $V_r^{\rm pinch}$ term is much larger than the V_r term, which represents the effect of neutral fuelling. These results imply that transport physics plays a much larger role in determining the shape of the density profile than does the fuelling profile.

There were at least two experimental observations from the JRT research that suggest that neutral fuelling might play an important role. One observation, previously noted, was that lithium deposition in NSTX produced a marked change in the density profile (figure 13) [37, 83]. Simulations with a 2D-edge code showed that in order to match the divertor D_α signals, the recycling coefficient had to be reduced from 0.98 without lithium to 0.9 with lithium [37]. The reduction in recycling was caused by pumping of deuterium by the lithium. As a result, the total particle source in the pedestal region was reduced by about 50% with the use of lithium. These results provide strong evidence that the details of the particle source play an important role in producing the structure of the density profile. This interpretation is rather different than that obtained from the paleoclassical model, noted above, in which changes of transport would be much more important than changes in the source. Taken together, these results might indicate that fuelling modifies the density profile both by playing a role in particle transport as well as by providing the particle source.

The second observation, indicating an important role for neutral fueling in setting the shape of the density profile,

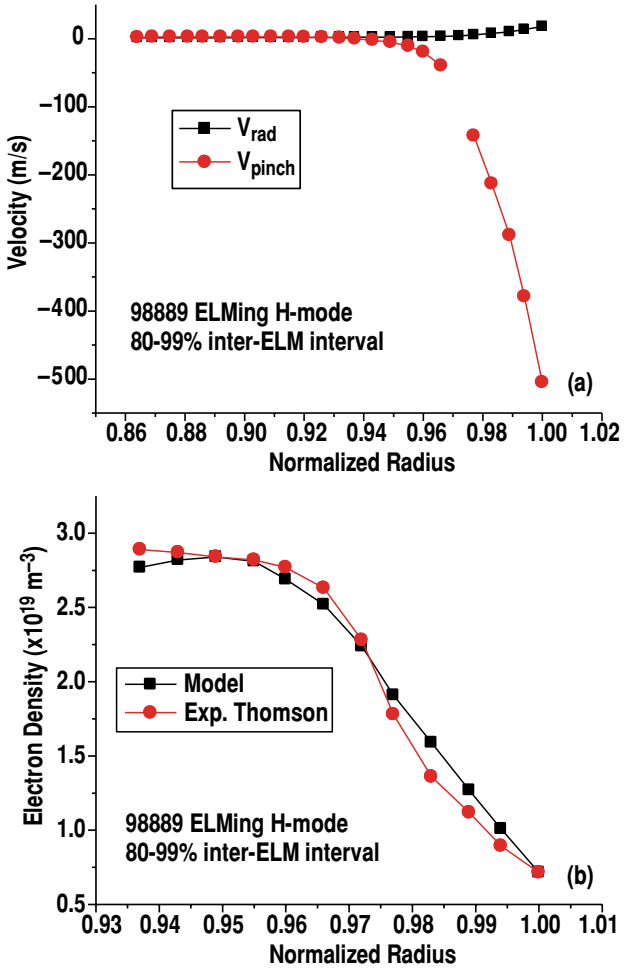

Figure 19. (*a*) Spatial variation of radial ion velocity V_r (squares) and generalized pinch velocity V_r^{pinch} (circles), as discussed in the text, for DIII-D discharge 98889; (*b*) spatial variation of experimental electron density (circles) and modelled density (squares) obtained from interpretive analysis based on combined constraints of momentum and particle balance. (Adapted with permission from [82]. Copyright 2012 by IOP Publishing and International Atomic Energy Agency.

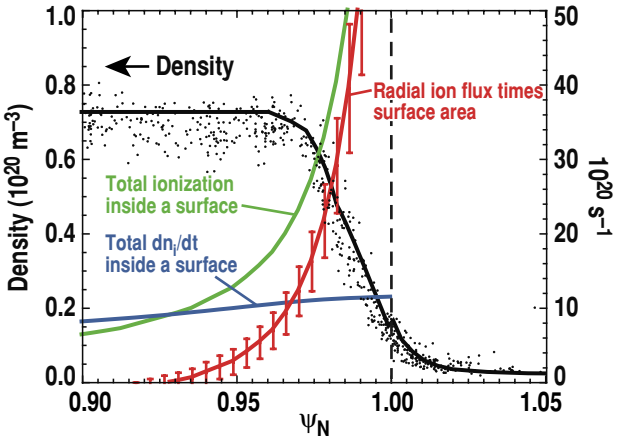

Figure 20. Spatial profiles of terms in the volume integral of particle balance equation $\Gamma_\perp(\psi)A = \int_0^\psi (S - \partial n/\partial t)\,\mathrm{d}V$, where $\Gamma_\perp(\psi)A$ = perpendicular ion flux times surface area, $\int_0^\psi S\,\mathrm{d}V$ = total ionization inside a surface and $\int_0^\psi (\partial n/\partial t)\,\mathrm{d}V$ = total $\mathrm{d}n_\mathrm{i}/\mathrm{d}t$ inside a surface. Units for these quantities are shown on right-hand vertical axis. Data points are experimental measurements of electron density and the fit curve is modelled density, obtained from OEDGE analysis of a DIII-D discharge. Units of density are shown on left-hand vertical axis.

was a pedestal similarity experiment performed in ELMing discharges in C-Mod and DIII-D. The goal of the experiment was to produce pedestals with the same dimensionless parameters (shape, q, collisionality, beta) on the pedestal top and this was achieved. As a result, the properly scaled T_e profiles matched but the scaled density profile in DIII-D was somewhat broader than in C-Mod. This result suggests that fueling was important in setting the density shape, given the expectation that the fueling profiles were quite different in the two machines. This result is in contrast to a similarity experiment between the two machines in which the density and temperature profiles were matched in EDA H-mode conditions [84].

Studies were performed on DIII-D with the goal of providing definitive experimental proof that an inward particle pinch exists inside the pedestal [85]. These studies evaluated the ion continuity equation $\nabla \cdot \Gamma = S - \partial n/\partial t$ to determine where in the plasma the flow of particles reversed from net outwards to net inwards. In this equation, Γ is the particle flux, S is the ionization rate (including ionization of beam particles and neutrals from the wall), n is the ion density and t is time. This equation can be integrated over volume V to provide the rate at which particles flow through a flux surface, $\Gamma_\perp(\psi)A = \int_0^\psi (S - \partial n/\partial t)\,\mathrm{d}V$, where ψ is normalized poloidal flux at the outermost surface of the integral, $\Gamma_\perp(\psi)$ is the particle flux through that surface and A is the area of that surface. The ionization rate of wall neutrals was obtained from interpretive analysis with the OEDGE code [86]. Details of the full analysis procedure are discussed elsewhere [85]. Figure 20 shows the results for the three terms in the volume-integrated continuity equation, as determined from this analysis for a discharge with a long ELM cycle, which allowed for good time history measurements of density evolution. The radial ion flux is positive (outwards) for ψ_N greater than 0.93 and becomes negative (inwards) at smaller radii, where the volume integral of the ionization source cannot account for the increase in the total number of ions inside a flux surface. The negative flux is interpreted as a sign of an inward particle pinch. However, in the pedestal, a pinch cannot be inferred from this analysis. This result does not rule out the possibility of a pinch in the pedestal. This research underscores the difficulties of experimentally proving that there is a pinch in the pedestal.

4. Summary and discussion

Joint experiment/theory/modelling research has led to improved understanding of the limits to the H-mode pedestal pressure profile, increased confidence in predictions of the pedestal height in ITER and new tests of models for pedestal temperature and density profiles. This work was performed as part of a US DOE Joint Research Target in fiscal year 2011 and included experimental research from C-Mod, DIII-D and NSTX as well as interpretation of experimental data with several theory-based modelling codes. The goal of

the research was to identify important physics processes that control pedestal structure and work towards improved predictive capability.

Two significant results of this work are that theoretical constraints on the pedestal pressure profile are consistent with a wide range of observations in these three machines and these constraints provide a good basis for understanding and predicting the pressure profile. The interplay between the total pressure profile and the edge current density profile, with a large contribution from the bootstrap current, provides the dominant physics for these constraints. One constraint is set by ideal finite-n peeling–ballooning modes, which are non-local modes, predicted to be the MHD modes that trigger type-I ELMs. Significant work was performed to extend models for these modes to the high-field C-Mod device and the low aspect ratio NSTX device. In all three machines, within error bars, the operating space is never observed to extend past the instability boundaries predicted for these modes.

The second constraint is that kinetic ballooning modes provide a limit to the local pedestal pressure gradient. These modes are smaller scale and less virulent than peeling–ballooning modes. However, these modes are predicted to turn on robustly when a critical pressure gradient is reached and to limit the gradient to near the critical value. Kinetic ballooning physics has provided a successful quantitative description of the pedestal width scaling in C-Mod and DIII-D. The model qualitatively captures the experimental trend that widths are higher in the low aspect ratio NSTX device than in the conventional aspect ratio machines.

These two constraints on the pedestal pressure profile have been combined into one model (EPED) which predicts pedestal width and height at the onset of a type-I ELM. The model makes good predictions of the pedestal pressure widths and heights observed in C-Mod and DIII-D over a wide range of conditions. The C-Mod data have increased the highest pressure at which the model has been tested by a factor of two. A new DIII-D data set has provided improved tests of the model at large widths. These predictions are accurate to about 20% and provide a good basis for predicting the pedestal height in ITER, which is predicted to have a pressure that is an extrapolation of a factor of 3 from the existing data set.

An important input to peeling–ballooning models and kinetic ballooning models is the current density profile, which is typically obtained from calculations using neoclassical bootstrap current models such as the Sauter model. New kinetic models with more complete physics have been used to compute the bootstrap current. Predictions of the Sauter model are in general agreement with the newer models for sufficiently collisionless conditions. However, there are often differences for collisional pedestals. An important open issue is that measurements of the edge current density are needed to benchmark predictive models.

Searches for the presence of kinetic ballooning modes have been performed in both experiment and simulations. Density fluctuations have been reported in some experiments that have signatures expected of kinetic ballooning modes, including frequency, localization to the pedestal and propagation direction. There have also been observations that the rate of change of the pedestal electron pressure gradient slows or is halted at the time that density fluctuations turn on in the pedestal. These observations are consistent with expectations for KBMs but it has not been shown that they are indeed caused by KBMs. Simulations have been performed for NSTX and DIII-D with electromagnetic gyrokinetic codes to determine if experimental profiles are unstable to KBMs. For calculations with a local model, KBMs have been found to be either subdominant to faster growing modes or to lie in a region expected to be second stable to these modes. In a global calculation, the modes were found to be unstable when the experimental reconstructed q-profile was artificially flattened. More experimental and simulation work is needed to clarify whether these modes play a role in the pedestal.

A number of models for other physics processes, particularly those relating to the structure of density or temperature profiles were also tested. The XGC0 code, employing models for kinetic ions and neutral fueling, has been used to examine the combined effect of neoclassical transport and neutral fueling on the density pedestal. The code qualitatively reproduces several features of the experiments, including the steep density gradients observed in the H-mode pedestal but typically produces density pedestals that are usually narrower than observed. Some anomalous particle transport is required in addition to neoclassical transport to explain the observations.

An analytic model for paleoclassical transport has been used to predict features of pedestal electron temperature and density profiles in NSTX and DIII-D. The model has made good predictions of the electron thermal diffusivity and the shape of the pedestal density profile in NSTX discharges with significant lithium injection. For a range of discharges in DIII-D, the model predicts the minimum observed electron thermal diffusivity. In other cases, additional electron thermal transport must be invoked to explain the results. The model predicts densities that are typically about 2 times larger than observed in DIII-D. Thus, some additional particle transport must be invoked to explain the observations.

There are qualitative and quantitative observations in all machines that have features expected for ETG modes, predicted to limit the pedestal T_e gradient. For instance, the ratio of the electron density scale length to the electron temperature scale length in the pedestal is $\sim$1–3, a magnitude that is expected to destabilize ETG modes. In addition, short wavelength fluctuations, in a range expected for ETG modes, have been observed at the edge of both NSTX and DIII-D. So far, though, there is no clear measurement of the amount of transport driven by ETG modes. Thus, they remain as candidates for important pedestal processes.

Linear calculations with electromagnetic gyrokinetic codes have been made to identify important fluctuation processes in and near the pedestal. These efforts find evidence of ITG and/or microtearing instabilities on the pedestal top and smaller scale, electron modes in the steep gradient region of the pedestal. However, the results are complex and machine-dependent and it is not yet clear if there is a consistent set of modes present in and on top of the pedestal. This work showed that edge magnetic geometry is important in the physics of these instabilities and must be properly modelled for accurate results. Simulations of EDA discharges in C-Mod with a two-fluid turbulence code predict that unstable modes exist in the pedestal when the resistivity is high. These modes have several

characteristics of the quasi-coherent (QC) modes observed in the C-Mod pedestal in these discharges.

Experimental and modelling evidence suggest that both atomic physics and a pinch play a role in controlling the density pedestal. Some of the strongest evidence in favour of a pinch is interpretive modelling, based on combined constraints of particle and momentum balance, which implies that a strong inward force plays a dominant role in molding the density profile. Some of the strongest evidence in favour of fueling was an experiment in NSTX in which the density profile shape was dramatically changed when the deuterium recycling coefficient was reduced by about an order of magnitude. However, it has so far not been possible to directly measure a pinch in the pedestal in experiments. In combination, these results suggest that both transport (pinch) and fueling effects play a role in the density profile shape and that the importance of these effects may be regime dependent.

Overall, these results provide increased confidence that some elements of pedestal structure (P-B stability, bootstrap current and pedestal gradient limits) are sufficiently well understood to allow for an understanding of limits to the pedestal pressure profile. This understanding can be used to predict the pedestal height in ITER with good confidence. For the ITER baseline scenario, the predicted pedestal temperature is in the range needed to get fusion $Q = 10$, as implied by several transport models [1]. In addition, this understanding provides the important ability to perform pedestal optimization studies in existing and future machines. An important next step for pedestal modelling is an understanding of the physics of the density and/or temperature profile. A predictive capability for one or both of these profiles will provide a more complete and powerful capability for designing and optimizing the next generation of machines.

Acknowledgments

This work was supported in part by the US Department of Energy under DE-FC02-04ER54698, DE-FG02-95ER54309, DE-FG02-00ER54538, DE-AC52-07NA27344, DE-FC02-93ER54186, DE-AC05-00OR22725, DE-AC02-09CH11466, DE-AC04-94AL85000, DE-FG03-94ER54271, DE-FG02-08ER54984, DE-FG02-07ER54917, DE-FC02-05ER54816, DE-FG02-89ER53296, DE-FG02-08ER54999 and work performed at the University of Toronto was funded by the Natural Sciences and Engineering Research Council of Canada.

References

[1] Doyle E.J. *et al* 2007 Progress in the ITER Physics Basis: chapter 2. Plasma confinement and transport *Nucl. Fusion* **47** S18
[2] Chan V.S. *et al* 2011 *Nucl. Fusion* **51** 083019
[3] Snyder P.B., Groebner R.J., Leonard A.W., Osborne T.H. and Wilson H.R. 2009 *Phys. Plasmas* **16** 056118
[4] Osborne T.H., Groebner R.J., Lao L.L., Leonard A.W., Maingi R., Miller R.L., Porter G.D., Thomas D.M. and Waltz R.E. 1997 *Proc. 24th EPS Conf. on Controlled Fusion and Plasma Physics (Berchtesgaden, Germany, 1997)* vol 21A (Petit-Lancy: European Physical Society) p 1101
[5] Greenwald M. *et al* 1997 *Nucl. Fusion* **37** 793
[6] Suttrop W. *et al* 1997 *Plasma Phys. Control. Fusion* **39** 2051
[7] Kotschenreuther M., Dorland W., Liu Q.P., Hammett G.W., Beer M.A., Smith S.A., Bondeson A. and Cowley S.C. 1997 *Proc. 16th Int. Conf. on Fusion Energy 1996 (Montreal, Canada, 1996)* vol 2 (Vienna: IAEA) p 371 and www-naweb.iaea.org/napc/physics/FEC/STIPUB1004_VOL2.pdf
[8] Kinsey J.E., Bateman G., Onjun T., Kritz A.H., Pankin A., Staebler G.M. and Waltz R.E. 2003 *Nucl. Fusion* **43** 1845
[9] Kinsey J.E., Staebler G.M., Candy J., Waltz, R.E. and Budny R.V. 2011 *Nucl. Fusion* **51** 083001
[10] Snyder P.B. *et al* 2012 *39th EPS Conf. on Plasma Physics and 16th Int. Congress on Plasma Physics 2012 (Stockholm, Sweden)* vol 36F (Madrid: European Physical Society) P4.029 and http://ocs.ciemat.es/epsicpp2012pap/html/
[11] Snyder P.B. *et al* 2009 *Nucl. Fusion* **49** 085035
[12] Sauter O., Angioni C. and Lin-Liu Y.R. 1999 *Phys. Plasmas* **6** 2834
[13] Houlberg W.A., Shaing K.C., Hirshman S.P. and Zarnstorff M.C. 1997 *Phys. Plasmas* **4** 3230
[14] Wade M.R., Murakami M. and Politzer P.A. 2004 *Phys. Rev. Lett.* **92** 235005
[15] Thomas D.M., Leonard A.W., Groebner R.J., Osborne T.H., Casper T.A., Snyder P.B. and Lao L.L. 2005 *Phys. Plasmas* **12** 056123
[16] De Bock M.F.M., Citrin J., Saarelma S., Temple D., Conway N.J., Kirk A., Meyer H., Michael C.A. and the MAST Team 2012 *Plasma Phys. Control. Fusion* **54** 025001
[17] Chang C.S., Ku S. and Weitzner H. 2004 *Phys. Plasmas* **11** 2649
[18] Belli E.A. and Candy J. 2008 *Plasma Phys. Control. Fusion* **50** 095010
[19] Landreman M. and Ernst Darin R. 2012 *Plasma Phys. Control. Fusion* **54** 115006
[20] Koh S., Chang C.S., Ku S., Menard J.E., Weitzner H. and Choe W. 2012 *Phys. Plasmas* **19** 072505
[21] Chang C.S., Koh S., Choe W., Ku S., Parker S., Wan W. and Chen Y. 2012 *Proc. 24th Int. Conf. on Fusion Energy 2012 (San Diego, CA, 2012)* TH/P4-12 and www-naweb.iaea.org/napc/physics/FEC/FEC2012/index.htm
[22] Hirshman S.P. 1988 *Phys. Fluids* **31** 3150
[23] Callen J.D. 2010 Viscous forces due to collisional parallel stresses for extended MHD codes Univ. Wisconsin Reports UW-CPTC 09-6R; 2011 Parallel neoclassical resistivity evaluation Univ. Wisconsin Reports UW-CPTC 11-05
[24] Pankin A.Y. *et al* 2012 *Proc. 24th Int. Conf. on Fusion Energy 2012 (San Diego, CA, 2012)* TH/P4-07 and www-naweb.iaea.org/napc/physics/FEC/FEC2012/index.htm
[25] Hegna C.C., Connor J.W., Hastie R.J. and Wilson H.R. 1996 *Phys. Plasmas* **3** 584
[26] Hughes J.W., Mossessian D., Zhurovich K., DeMaria M., Jensen K. and Hubbard A. 2003 *Rev. Sci. Instrum.* **74** 1667
[27] Eldon D. *et al* 2012 *Rev. Sci. Instrum.* **83** 10E343
[28] LeBlanc B.P., Bell R.E., Johnson D.W., Hoffman D.E., Long D.C. and Palladino R.W. 2003 *Rev. Sci. Instrum.* **74** 1659
[29] McDermott R.M. *et al* 2009 *Phys. Plasmas* **16** 056103
[30] Gohil P., Burrell K.H., Groebner R.J., Kim J., Martin W.C., McKee E.L. and Seraydarian R.P. 1991 *Proc. 14th Symp. on Fusion Engineering (San Diego, CA)* vol 2 (New York: Institute of Electrical and Electronics Engineers) p 1199
[31] Bell R.E., Andre R., Kaye S.M., Kolesnikov R.A., LeBlanc B.P., Rewoldt G., Wang W.X. and Sabbagh S.A. 2010 *Phys. Plasmas* **17** 082507
[32] Lao L.L., Ferron J.R., Groebner R.J., Howl W., St. John H., Strait E.J. and Taylor T.S. 1990 *Nucl. Fusion* **30** 1035
[33] Osborne T.H., Snyder P.B., Burrell K.H., Evans T.E., Fenstermacher M.E., Leonard A.W., Moyer R.A., Schaffer M.J. and West W.P. 2008 *J. Phys.: Conf. Ser.* **123** 012014
[34] Walk J.R., Snyder P.B., Hughes J.W., Terry J.L., Hubbard A.E. and Phillips P.E. 2012 *Nucl. Fusion* **52** 063011

[35] Wilson H.R., Snyder P.B., Huysmans G.T.A. and Miller R.L. 2002 *Phys. Plasmas* **9** 1277
[36] Snyder P.B. and Wilson H.R. 2003 *Plasma Phys. Control. Fusion* **45** 1671
[37] Canik J.M. *et al* 2011 *Phys. Plasmas* **18** 056118
[38] Boyle D.P., Maingi R., Snyder P.B., Manickam J., Osborne T.H., Bell R.E., LeBlanc B.P. and the NSTX Team 2011 *Plasma Phys. Control. Fusion* **53** 105011
[39] Whyte D.G. *et al* 2010 *Nucl. Fusion* **50** 105005
[40] Hughes J. *et al* 2013 *Nucl. Fusion* **53** 043016
[41] Greenwald M. *et al* 1999 *Phys. Plasmas* **6** 1943
[42] Snyder P.B., Groebner R.J., Hughes J.W., Osborne T.H., Beurskens M., Leonard A.W., Wilson H.R. and Xu X.Q. 2011 *Nucl. Fusion* **51** 103016
[43] Miller R.L., Lin-Liu Y.R., Turnbull A.D., Chan V.S., Pearlstein L.D., Sauter O. and Villard L. 1997 *Phys. Plasmas* **4** 1062
[44] Groebner R.J., Leonard A.W., Snyder P.B., Osborne T.H., Maggi C.F., Fenstermacher M.E., Petty C.C. and Owen L.W. 2009 *Nucl. Fusion* **49** 085037
[45] Diallo A., Maingi R., Kubota S., Sontag A., Osborne T., Podestà M., Bell R.E., LeBlanc B.P., Menard J. and Sabbagh S. 2011 *Nucl. Fusion* **51** 103031
[46] Groebner R.J., Osborne T.H., Leonard A.W. and Fenstermacher M.E. 2009 *Nucl. Fusion* **49** 045013
[47] Groebner R.J. *et al* 2010 *Nucl. Fusion* **50** 064002
[48] Wolfrum E., Burckhart A., Fischer R., Hicks N., Konz C., Kurzan B., Langer B., Pütterich T., Zohm H. and the ASDEX Upgrade Team 2009 *Plasma Phys. Control. Fusion* **51** 124057
[49] Burckhart A., Wolfrum E., Fischer R., Lackner K., Zohm H. and the ASDEX Upgrade Team 2010 *Plasma Phys. Control. Fusion* **52** 105010
[50] Dickinson D., Saarelma S., Scannell R., Kirk A., Roach C.M. and Wilson H.R. 2011 *Plasma Phys. Control. Fusion* **53** 115010
[51] Snyder P.B., Osborne T.H., Burrell K.H., Groebner R.J., Leonard A.W., Nazikian R., Orlov D.M., Schmitz O., Wade M.R. and Wilson H.R. 2012 *Phys. Plasmas* **19** 056115
[52] Yan Z., McKee G.R., Groebner R.J., Snyder P.B., Osborne T.H. and Burrell K.H. 2011 *Phys. Rev. Lett.* **107** 055004
[53] Yan Z., McKee G.R., Groebner R.J., Snyder P.B., Osborne T.H., Beurskens M.N. and Burrell K.H. 2011 *Phys. Plasmas* **18** 056117
[54] McKee G.R., Fonck R.J., Gupta D.K., Schlossberg D.J., Shafer M.W., Boivin R.L. and Solomon W.M. 2007 *Plasma Fusion Research* **2** S1025
[55] Wang E., Xu X., Candy J., Groebner R.J., Snyder P.B., Chen Y., Parker S.E., Wan W., Lu G. and Dong J.Q. 2012 *Nucl. Fusion* **52** 103015
[56] Wan W., Parker S.E., Chen Y., Yan Z., Groebner R.J. and Snyder P.B. 2012 *Phys. Rev. Lett.* **109** 185004
[57] Canik J.M., Guttenfelder W., Maingi R., Osborne T.H., Kubota S., Ren Y., Bell R.E., Kugel H.W., LeBlanc B.P. and Souhkanovskii V.A. 2013 Edge plasma transport and microstability analysis with lithium-coated plasma-facing components in NSTX, *Nucl. Fusion* submitted
[58] Huysmans G.T.A, Goedbloed J.P and Kerner W.O.K 1991 *Int. J. Mod. Phys.* C **02** 371
[59] Kotschenreuther M., Rewoldt G. and Tang W.M. 1995 *Comput. Phys. Commun.* **88** 128
[60] Candy J. and Waltz R.E. 2003 *J. Comput. Phys.* **186** 545
[61] Chen Y. and Parker S.E. 2007 *J. Comput. Phys.* **220** 839
[62] Snyder P.B. *et al* 2012 *Proc. 24th Int. Conf. on Fusion Energy 2012 (San Diego, CA, 2012)* TH/P3-17 and www-naweb.iaea.org/napc/physics/FEC/FEC2012/index.htm
[63] Pankin A.Y. *et al* 2011 Kinetic modeling of H-mode pedestal with effects from anomalous transport and MHD stability *Problems of Atomic Science and Technology 2011 No. 1. Series: Plasma Physics* **(17)** 8–12
[64] Pankin A.Y. *et al* 2011 Stress tests of transport models using FACETS code *AIP Conf. Proc.* **1392** 110
[65] St John H., Taylor T.S., Lin-Liu Y.R. and Turnbull A.D. 1994 *Proc. 15th Int. Conf. on Plasma Physics and Controlled Nuclear Fusion Research 1994 (Seville, 1994)* vol 3 (Vienna: IAEA) p 60 www-naweb.iaea.org/napc/physics/FEC/STIPUB948_VOL3.pdf
[66] Callen J.D. 2005 *Nucl. Fusion* **45** 1120
[67] Callen J.D., Canik J.M. and Smith S.P. 2012 *Phys. Rev. Lett.* **108** 245003
[68] Smith S.P., Callen J.D., Groebner R.J., Osborne T.H., Leonard A.W., Eldon D., Bray B.D. and the DIII-D Team 2012 *Nucl. Fusion* **52** 114016
[69] ITER Physics Expert Group on Confinement, Transport, ITER Physics Expert Group on Confinement Modelling, Database, and ITER Physics Basis Editors 1999 Plasma confinement and transport *Nucl. Fusion* **39** 2175 chapter 2
[70] Dong J.Q., Guzdar P.N. and Lee Y.C. 1987 *Phys. Fluids* **30** 2694
[71] Miller L., Chu M.S., Green J.M., Lin-Liu Y.R. and Waltz R.E. 1998 *Phys. Plasmas* **5** 973
[72] Candy J. 2009 *Plasma Phys. Control. Fusion* **51** 105009
[73] Dong J.Q., Chen L., Zonca F. and Jian G.D. 2004 *Phys. Plasmas* **11** 997
[74] Xu X.Q., Cohen R.H., Rognlien T.D. and Myra J.R. 2000 *Phys. Plasmas* **7** 1951
[75] Dudson D., Umansky M.V., Xu X.Q., Snyder P.B. and Wilson H.R. 2009 *Comput. Phys. Commun.* **180** 1467
[76] Jenko F., Told D., Xanthopoulos P., Merz F. and Horton L.D. 2009 *Phys. Plasmas* **16** 055901
[77] Jenko F., Dorland W., Kotschenreuther M. and Rogers B.N. 2000 *Phys. Plasmas* **7** 1904
[78] Rhodes T.L., Peebles W.A., Nguyen X., Van Zeeland M.A., deGrassie J.S., Doyle E.J., Wang G. and Zeng L. 2006 *Rev. Sci. Instrum.* **77** 10E922
[79] Mahdavi M.A., Maingi R., Groebner R.J., Leonard A.W., Osborne T.H. and Porter G. 2003 *Phys. Plasmas* **10** 3984
[80] Kukushkin A.S., Pacher H.D., Loarte A., Komarov V., Kotov V., Merola M., Pacher G.W. and Reiter D. 2009 *Nucl. Fusion* **49** 075008
[81] Stacey W.M. and Groebner R.J. 2009 *Phys. Plasmas* **16** 102504
[82] Stacey W.M., Groebner R.J. and Evans T.E. 2012 *Nucl. Fusion* **52** 114020
[83] Maingi R. *et al* 2012 *Nucl. Fusion* **52** 083001
[84] Mossessian D.A., Groebner R.J., Moyer R.A., Osborne T.H., Hughes J.W., Greenwald M., Hubbard A., Rhodes T.L. 2003 *Phys. Plasmas* **10** 689
[85] Leonard A.W., Elder J.D., Canik J.M., Groebner R.J. and Osborne T.H. 2013 *J. Nucl. Mater.* **438** (Suppl.) S246–9
[86] Lisgo S. *et al* 2005 *J. Nucl. Mater.* **337–339** 139